

## Seasonality and weather-driven variability of transpacific transport

Mark Holzer<sup>1,2,3</sup> and Timothy M. Hall<sup>1</sup>

Department of Applied Physics and Applied Mathematics, Columbia University, New York, New York, USA

Roland B. Stull

Atmospheric Science Program, Department of Earth and Ocean Sciences, University of British Columbia, Vancouver, British Columbia, Canada

Received 23 May 2005; revised 24 August 2005; accepted 8 September 2005; published 3 December 2005.

[1] We quantify transport from the industrialized regions of E Asia using the transit-time probability density function,  $\mathcal{G}$ , to isolate the role of transport from any other factors, such as chemistry and deposition. Using the offline transport model MATCH driven by NCEP reanalyses, we calculate  $\mathcal{G}$ , which is the mass fraction of air that had its last contact with the E-Asian source region during a given day, for each day of a three-year period. Ensemble means of  $\mathcal{G}$  establish the climatological seasonal-mean transport from E Asia. Export from the source region is most efficient in spring, with nearly all E-Asian air involved in transpacific transport. In summer, E-Asian air is transported aloft across the Pacific and, in nearly equal measure, west over SE Asia to the Middle East. Winter transport is similar to that of spring, except winter has low-level transport to SE Asia. Fall transport is intermediate between that of summer and winter. For all seasons, the most probable transit times to N America are 6–8 days in the mid-to-upper troposphere and approximately one week (two for summer) longer at the surface. The surface signal of E-Asian air over N America is strongest in spring. Daily variability of transpacific transport is quantified in terms of the transit-time partitioned burden of E-Asian air over western N America. The standard deviation of the transit-time partitioned fluctuations has a nearly universal dependence on the corresponding seasonal-mean burden. The standard deviation peaks several days before the burden at a transit time of  $\sim 7$  days. Lagged event and nonevent composites, based on the western N-American burden of E-Asian air, reveal that transport events are associated with dipolar wind perturbations over the eastern Pacific that are positioned and phased to receive enhanced Asian outflow. Surface-pressure correlations are consistent with an associated strengthened Pacific High and weakened Aleutian Low.

**Citation:** Holzer, M., T. M. Hall, and R. B. Stull (2005), Seasonality and weather-driven variability of transpacific transport, *J. Geophys. Res.*, 110, D23103, doi:10.1029/2005JD006261.

### 1. Introduction

[2] It is becoming evident that long-range, inter-continental transport of pollutants plays an important and growing role in determining atmospheric composition and air quality at populated locations remote from the sources. A large body of observational evidence exists for transpacific trans-

port, in part because of spectacular dust events that have drawn attention to the phenomenon [e.g., Merrill *et al.*, 1989; Husar *et al.*, 2001; McKendry *et al.*, 2001; Tratt *et al.*, 2001; Uno *et al.*, 2001; Vaughan *et al.*, 2001] and more importantly because E Asia is a large and rapidly growing source of industrial pollutants, which have the potential to impact North-American air quality via long-range transport across the Pacific [e.g., Berntsen *et al.*, 1999; Jacob *et al.*, 1999; Jaeglé *et al.*, 2003; Hudman *et al.*, 2004].

[3] The Asian outflow of pollutants has been investigated during several recent spring-time aircraft campaigns to characterize its chemical structure and the meteorology of the export from the Asian continent (see Jacob *et al.* [2003] for an overview of TRACE-P (Feb.–April 2001) and Parrish *et al.* [2004] for an overview of PEACE-B (April–May 2002)). Export mechanisms have been classified in terms of the air streams of frontal systems, particu-

<sup>1</sup>Also at NASA Goddard Institute for Space Studies, New York, New York, USA.

<sup>2</sup>Also at Atmospheric Science Program, Department of Earth and Ocean Sciences, University of British Columbia, Vancouver, British Columbia, Canada.

<sup>3</sup>Also at Physics Department, Langara College, Vancouver, British Columbia, Canada.

larly lifting in warm conveyor belts [e.g., *Stohl*, 2001; *Liu et al.*, 2003] and boundary-layer outflow associated with cold fronts [e.g., *Liang et al.*, 2004]. *Cooper et al.* [2004] track merging air streams through a sequence of baroclinic systems across the Pacific during a particular transport event.

[4] A host of measurements from aircraft over the US west coast and from ground stations (notably Cheeka Peak in Washington state and Trinidad Head in northern California), coupled with either simple back trajectories or forward predictions from global chemical transport models, have shown that Asian pollution contributes to western N American background levels, and causes episodic enhancements of a number of species such as carbon monoxide (CO), ozone (O<sub>3</sub>), and fine particulates [e.g., *Jaffe et al.*, 1999, 2001, 2003; *Kotchenruther et al.*, 2001; *Heald et al.*, 2003; *Price et al.*, 2003].

[5] Transpacific transport is episodic [e.g., *Yienger et al.*, 2000; *Holzer et al.*, 2003] and strongest during spring, so that it is natural that most of the studies cited deal with measurements and modeling of particular springtime transport events and pollution episodes. Much less effort has been devoted to systematically quantifying the year-round transpacific transport climate, that is, the contribution of E-Asian air to the climatological background over remote receptor regions and the variability around the climatological mean. *Stohl et al.* [2002] used a one-year simulation with a Lagrangian particle dispersion model to study the intercontinental transport of a CO-like passive tracer in terms of transport timescales and pathways. *Holzer et al.* [2003] applied a transit-time probability-density-function (pdf) approach to quantify the spring-time transport climate from E Asia and to identify transport events objectively. *Liang et al.* [2004] use CO simulations from the GEOS-CHEM model [*Bey et al.*, 2001] to analyze a 15-month record of CO measurements from Cheeka Peak observatory in terms of transport events and import/export mechanisms. *Liu et al.* [2005] use simulations of O<sub>3</sub> to study the seasonal and interannual variability of monthly mean fluxes and their correlations with various sea-level pressure indices. *Liang et al.* [2005] use simulations of CO and correlations with sea-level pressure indices to study daily to interannual variability of Asian outflow and transpacific transport of CO.

[6] In this work we aim to isolate the role of transport from all the other factors determining the mixing ratio of actual trace species, such as chemistry and deposition. To that end we use a tracer-independent transport diagnostic, namely the transit-time probability density function (pdf) [*Hall and Plumb*, 1994; *Holzer and Hall*, 2000], which partitions the mass fraction of air that had its last contact with a specified surface region according to the transit time from that region. This approach improves on simple back trajectories because the advective-diffusive character of atmospheric transport is naturally built into the framework, so that all possible paths from the contact region to the point of interest are taken into account. The transit-time pdf also gives a more complete characterization of transport than is possible with any single chemical trace species. While tracers such as CO and O<sub>3</sub> do provide valuable transport information, their transport signature must be disentangled

from the effects of chemistry such as loss due to oxidation with hydroxyl radical (OH), whose concentration is highly variable and uncertain. Furthermore, the mixing ratio of these species at a point represents an aggregate of fluid elements that have had widely varying transit times and paths from their source regions. As a result, the transport signature of CO, with its ~2-month decay time, and that of O<sub>3</sub>, with its ~2-week decay time, are expected to be very different, especially in terms of their weather-driven variability. The transit-time pdf allows us to determine systematically which timescales dominate the variability of any particular species.

[7] This paper extends the work of *Holzer et al.* [2003] on transpacific springtime transport. The transit-time approach is computationally demanding, requiring over a thousand time-evolving tracers for a three-year climatology that resolves daily variability. We, therefore, focus on transport from a single region (denoted by  $\Omega$ ) that encompasses the major sources of E-Asian industrial pollution. We establish the climatological transport of air from  $\Omega$  (“ $\Omega$  air”) for all seasons and then systematically quantify the seasonality and day-to-day variability of  $\Omega$  air over western N America. The transit-time-partitioned time series of the  $\Omega$ -air burden over western N America is then used to form lagged, weighted composites of the wind fields and  $\Omega$  air corresponding to effective and ineffective transpacific transport. The composites are consistent with the correlation analysis of *Holzer et al.* [2003] for spring but directly distinguish unusually effective transpacific transport from the remainder of the ensemble for all seasons. The analysis suggests that effective transpacific transport requires enhanced export from the Asian continent that is appropriately phased with a dipolar wind perturbation over the eastern Pacific. The dipole receives the E-Asian air, shapes it into filaments, and then expels it onto western N America.

## 2. Transit-Time pdf and Numerical Implementation

[8] As in *Holzer et al.* [2003], we base our analysis on the transit-time pdf,  $\mathcal{G}$ , which is defined so that  $\mathcal{G}(\mathbf{r}, t|\Omega, t')d\mathbf{r}$  is the mass fraction of an air parcel at point  $\mathbf{r}$  and time  $t$  that had last contact with the surface patch,  $\Omega$ , during the time interval  $(t', t' + dt')$ . In this paper we concentrate on the E-Asian “pollution” region  $\Omega$ , as defined by *Holzer et al.* [2003] (see Figure 1) using sulfur dioxide emissions as a proxy for industrialization. This  $\Omega$  (denoted  $\Omega_P$  in *Holzer et al.* [2003]) has an area of  $3.74 \times 10^6$  km<sup>2</sup> and a mean elevation of 696 m.

[9] To compute  $\mathcal{G}$ , we use MATCH (Model of Atmospheric Transport and Chemistry), a three-dimensional global model of the atmosphere developed by *Rasch et al.* [1997]. MATCH uses the mass-conserving SPITFIRE (Split Implementation of Transport Using Flux Integral Representation) flux algorithm [*Rasch and Lawrence*, 1998]. We drive MATCH with T63 NCEP reanalysis data [*Kalnay et al.*, 1996; *Kistler et al.*, 2001] at the resolution of the data: a Gaussian grid of 94 latitudes and 192 longitudes ( $\sim 1.9^\circ \times 1.9^\circ$ ), with 28 hybrid levels up to  $\sim 3$  mb.

[10] The transit-time pdf,  $\mathcal{G}$ , is calculated as the response to a pulse in mixing ratio on  $\Omega$ . We emphasize that

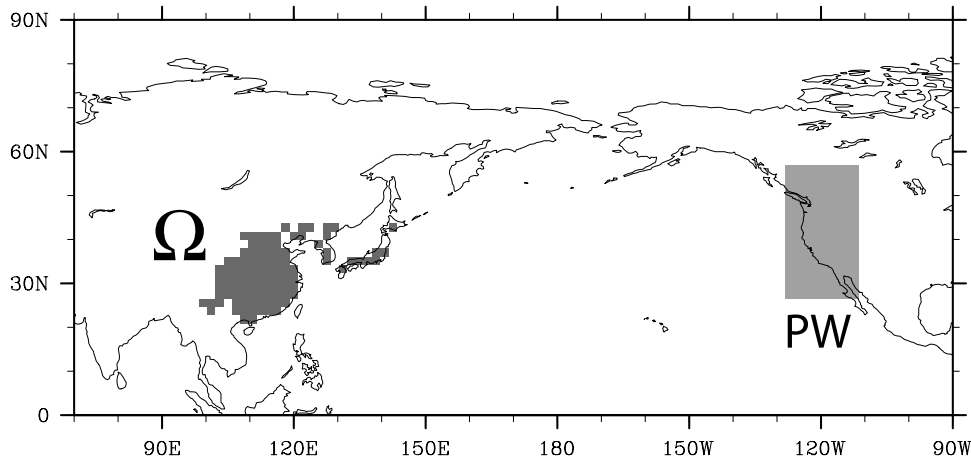


**Figure 1.** The east-Asian contact region,  $\Omega$ , used to calculate the air-mass fraction  $\mathcal{G}(\mathbf{r}, t|\Omega, t') dt'$  at  $(\mathbf{r}, t)$  that had last contact with  $\Omega$  during the interval  $(t', t' + dt')$ . Our choice for  $\Omega$  is based on the fact that air making contact with this region is likely to be labeled with pollution. To quantify the variability of E-Asian transport, we focus on the PW receptor region.

boundary conditions on  $\Omega$  are specified in terms of mixing ratio and not in terms of emission fluxes. In practice, mixing ratio is specified in MATCH for the lowest model level over  $\Omega$  as a day-long, 00Z to 00Z, square pulse of amplitude 1/day. The response at time  $t$  (the “field time”) to such a pulse that occurred during day  $t'$  (the “source time”) gives the mass fraction of air at time  $t$  that had its last contact with  $\Omega$  during the 24-hr period of day  $t'$ . Elsewhere on the surface, we enforce zero-flux boundary conditions for  $\mathcal{G}$ , as in *Holzer et al.* [2003].

[11] The transit-time pdf,  $\mathcal{G}$ , is in principle physically and conceptually distinct from the spectra of “literal” tracer age (time since emission) calculated by *Stohl et al.* [2002] using Lagrangian particles. Each particle is labeled by emission date and source region, and the label is not reset when the particle makes subsequent contact with the source region. Therefore, the spectra of the time since emission do not have a natural, time-independent normalization. In particular, the mean time since emission depends on the maximum time for which particles are tracked and increases without bound with this maximum time. By contrast,  $\mathcal{G}$  represents the normalized distribution of transit times since fluid elements had last contact with  $\Omega$  at time  $t = t'$ , when they were labeled with their current physical mixing ratio. Mixing-ratio information from prior contact with  $\Omega$  is thus reset with every  $\Omega$  contact, regardless of when the trace gases were injected into the atmosphere. For  $\mathcal{G}$  this resetting is accomplished by its boundary conditions, which remove the  $\Omega$  label from fluid elements that make  $\Omega$  contact for  $t > t'$ . It turns out, however, that for the transit times of interest here (order several weeks), having a small contact patch (such as our E-Asian  $\Omega$ ) results in little difference between the literal age spectra of *Stohl et al.* [2002] and the transit-time pdf at locations far from  $\Omega$ . Once air has escaped the boundary layer over the source region, it has little chance of contacting the source region within a few weeks. For an analysis of the differences between the two types of distribution, see *Holzer and Hall* [2000].

[12] A key property of  $\mathcal{G}$  is that it is a propagator of time-dependent, spatially uniform mixing ratio on  $\Omega$ . Given a

time series  $\chi_{\Omega}(t')$  for the mixing ratio of a species on  $\Omega$ , the mixing ratio at any point  $\mathbf{r}$  in the atmosphere can be obtained by the convolution

$$\chi(\mathbf{r}, t) = \int_{-\infty}^t dt' e^{-(t-t')/\tau_c} \mathcal{G}(\mathbf{r}, t|\Omega, t') \chi_{\Omega}(t'), \quad (1)$$

where we have inserted the factor  $\exp[-(t - t')/\tau_c]$  to account for species that undergo photochemical or radioactive decay with constant time constant  $\tau_c$ . In particular, if the mixing ratio on  $\Omega$  is constant,  $f(\mathbf{r}, t) \equiv \int_{-\infty}^t dt' e^{-(t-t')/\tau_c} \mathcal{G}(\mathbf{r}, t|\Omega, t')$  represents the mass fraction of an air parcel at  $\mathbf{r}$  that carries species  $\chi$ . A more complete discussion of the properties of the boundary propagator is given by *Holzer and Hall* [2000].

[13] To establish its climate, we compute  $\mathcal{G}(\mathbf{r}, t|\Omega, t')$  for three years of source days  $t'$  from September 1, 1998 to August 31, 2001. With the day-long source pulses used, we thus follow the three-dimensional evolution of 1096  $\mathcal{G}$  tracers. This gives us  $\sim 270$  realizations per three-month season, comparable to the 255 realizations used in *Holzer et al.* [2003] for 5 years of 51-day springtime periods. We compute the evolution of each  $\mathcal{G}$  for transit times  $\xi \equiv t - t'$  up to 30 days, and archive daily averages of  $\mathcal{G}$  and the corresponding meteorological fields.

### 3. Seasonality of the Climatological Mean Transit-Time pdf

[14] The climatological mean transit-time pdf,  $\langle \mathcal{G}(\mathbf{r}, t|\Omega, t') \rangle$ , is defined as the average over an ensemble of realizations of  $\mathcal{G}(\mathbf{r}, t|\Omega, t')$  at fixed transit time  $t - t'$  [*Holzer et al.*, 2003]. We consider seasonal ensembles corresponding to source times  $t'$  in a given three-month period for the three years available. We adopt the conventional three-month definitions for seasons: DJF, MAM, JJA, and SON. Figures 2–5 characterize  $\langle \mathcal{G} \rangle$  for each season. During all seasons, there is significant transport across the Pacific, although pronounced seasonality is apparent. The detailed evolution of  $\mathcal{G}(\mathbf{r}, t|\Omega, t')$ , or “ $\Omega$  air” for short, is

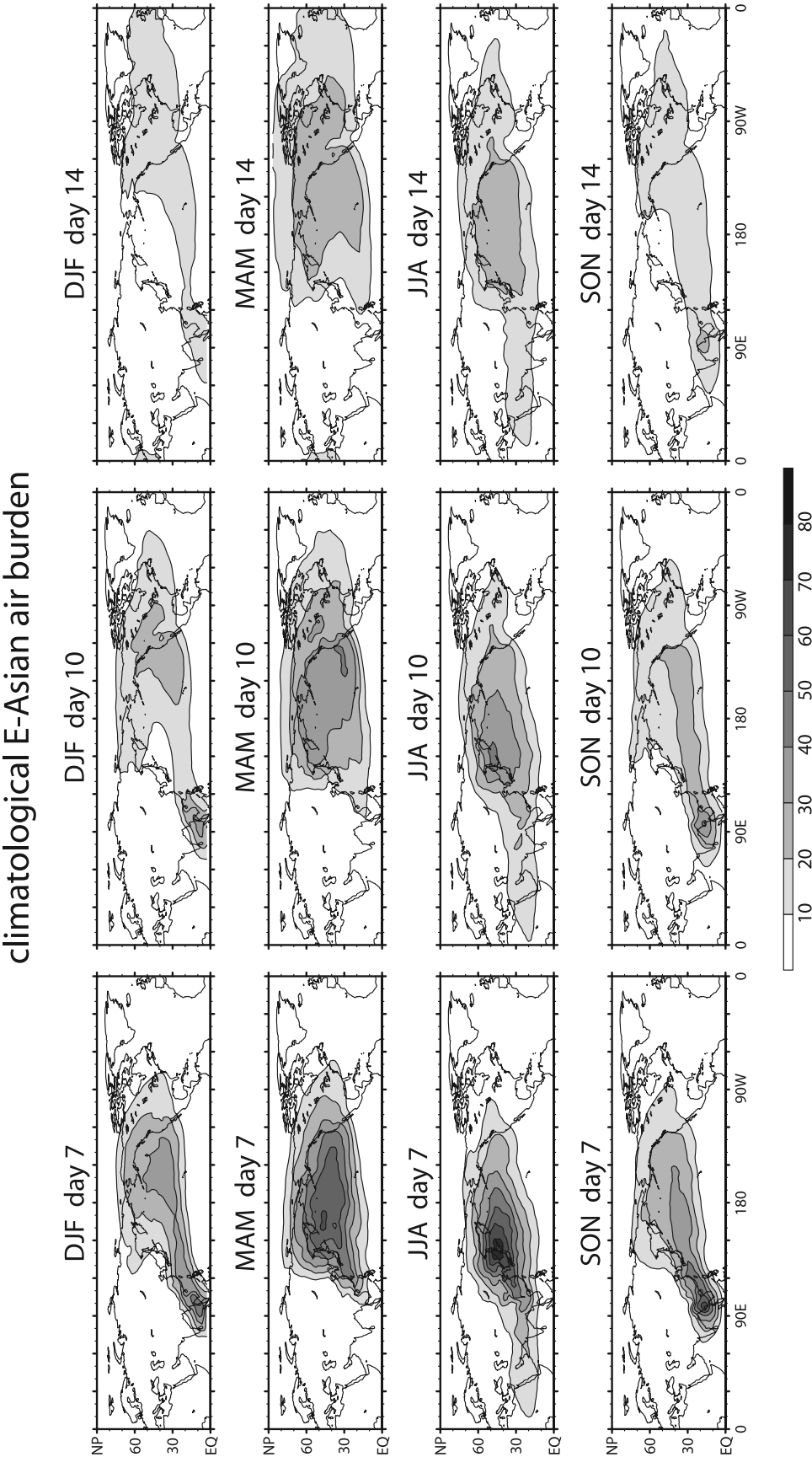


**Figure 2.** The climatological average burden in  $\text{kg m}^{-2}$  of E Asian air that had its last contact with the E Asian source region (Figure 1) during the 24-hour periods 7, 10, and 14 days ago for each season as indicated.



# NH meridional average E-Asian air-mass fraction

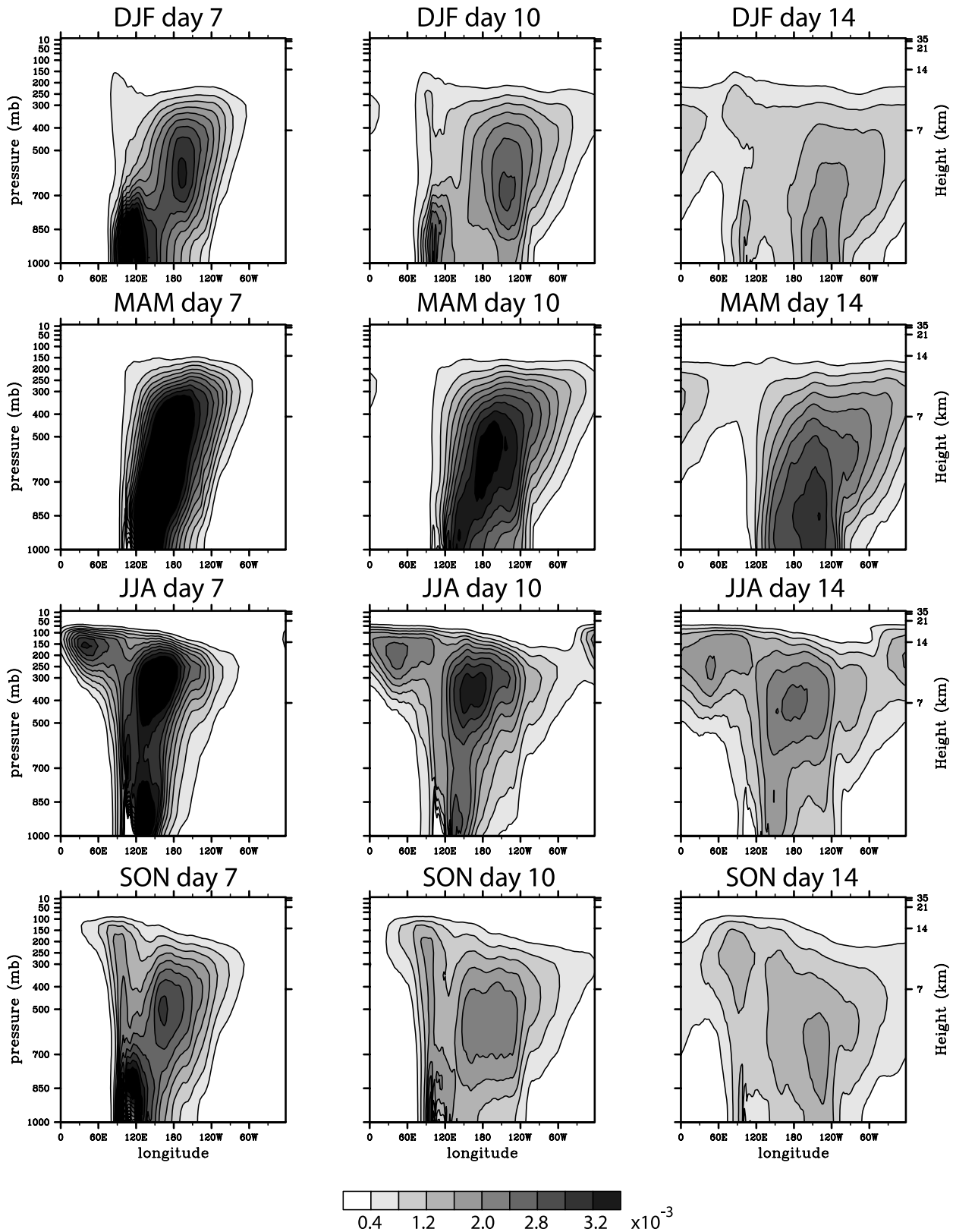


**Figure 3.** The climatological NH meridional average E-Asian air-mass fraction that had its last contact with the E-Asian source region (Figure 1) during the 24-hour periods 7, 10, and 14 days ago for each season as indicated.

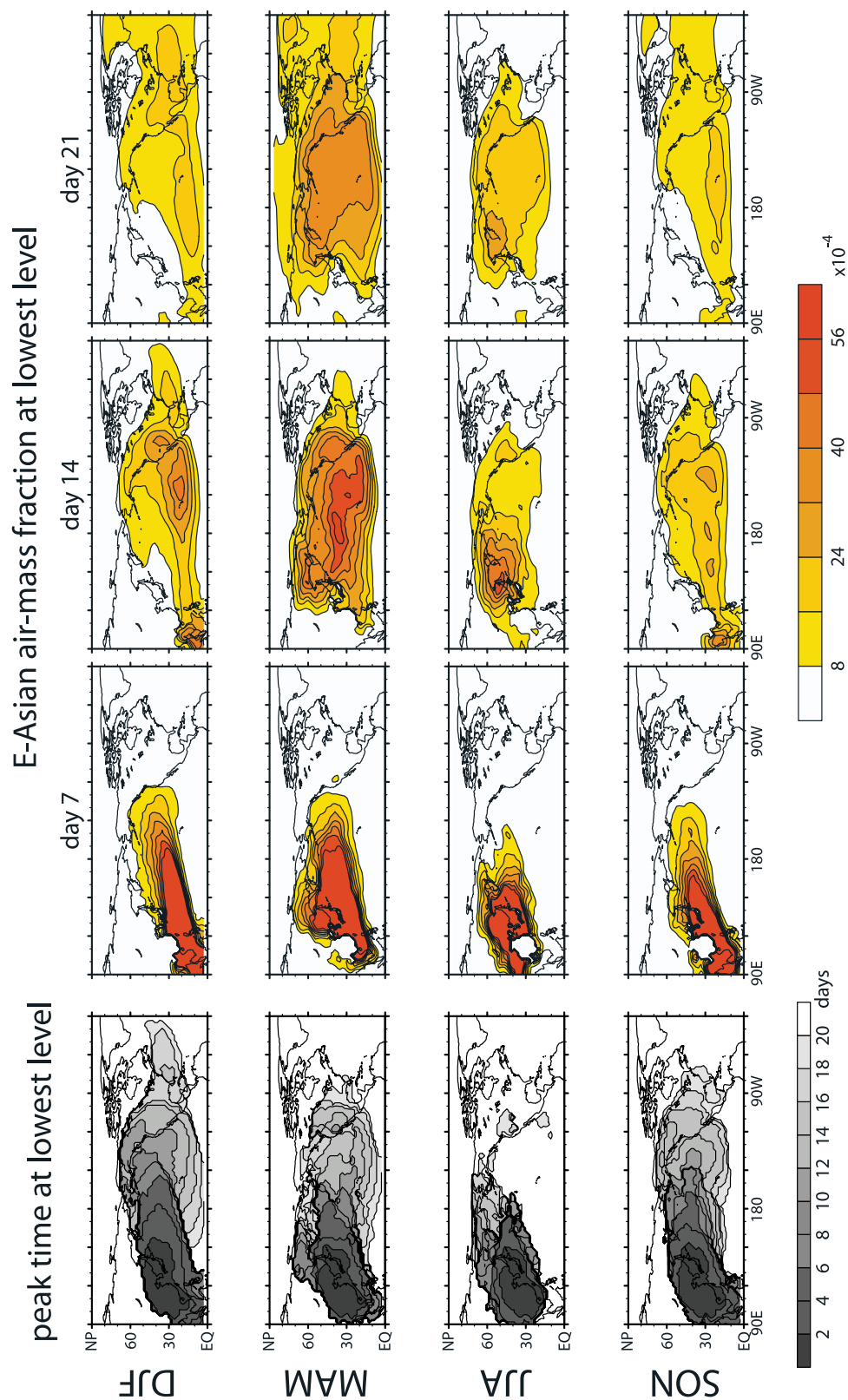


**Figure 4.** Leftmost panels: The peak time of the climatological E-Asian air-mass fraction at the surface (lowest model level) for all four seasons, as indicated. Colored panels: The climatological air-mass fraction at the surface that had its last contact with the E-Asian source region during the 24-hour periods 7, 14 and 21 days ago, as indicated for each season.

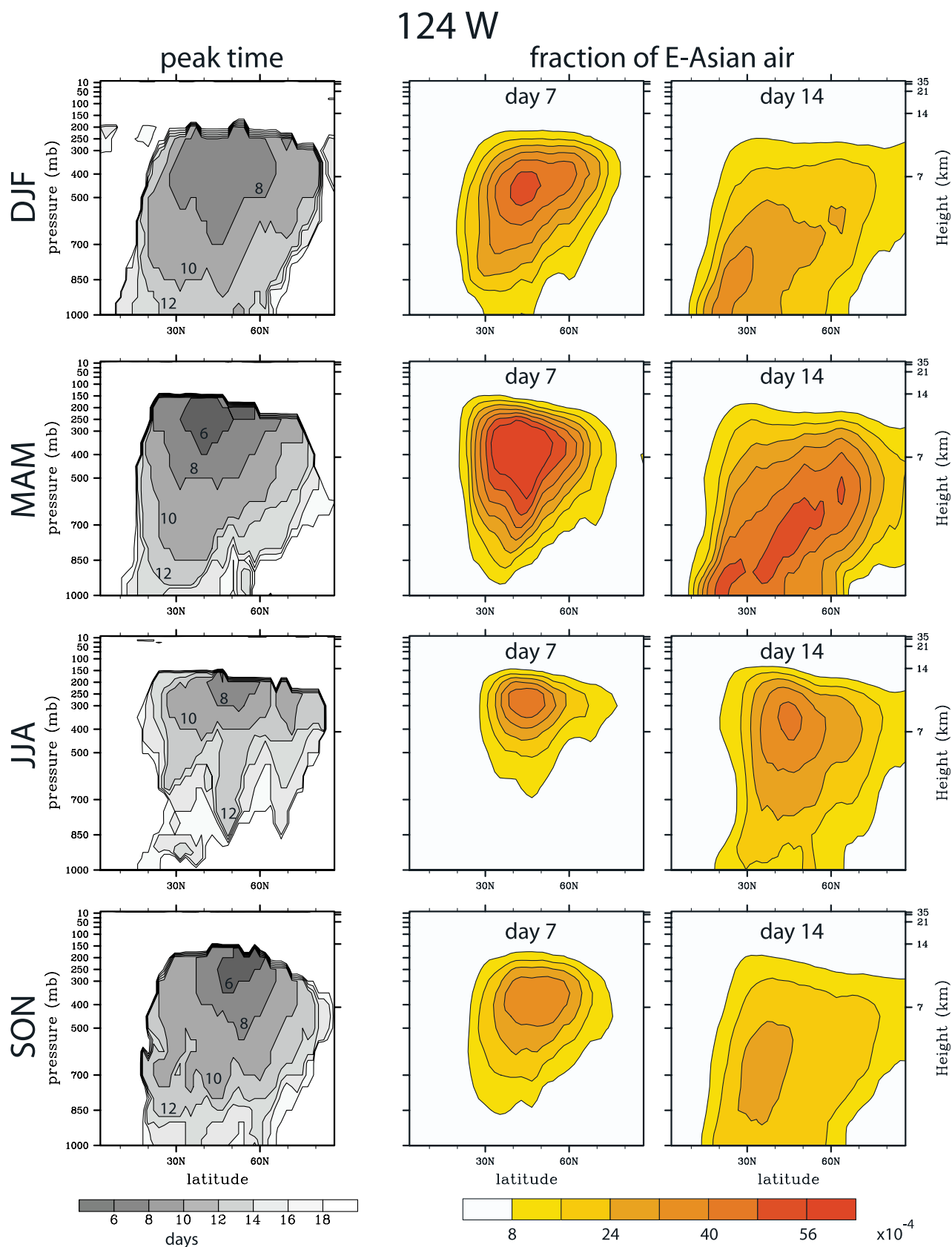


**Figure 5.** Pressure-latitude cross-sections through the northern hemisphere at 124°W for the peak time of the climatological average E-Asian air-mass fraction together with the climatological air-mass fraction that had its last contact with the E-Asian source region during the 24-hour periods 7 and 14 days ago, as indicated for each season.

complex even in the climatological average and we only attempt to describe some of the gross features of  $\langle G \rangle$  here for the  $\sim 2$  weeks since last  $\Omega$  contact, when the bulk of transpacific transport occurs.

### 3.1. Burden and Meridional Averages

[15] Figure 2 shows the ensemble averaged column burden  $\langle G \rangle \equiv \langle \int_0^{p_s} G dp/g \rangle$  ( $p$  is pressure,  $p_s$  surface pressure,  $g$  the acceleration of gravity). A summary of the vertical structure of the climatological evolution of  $\Omega$  air is provided by the NH meridional averages of Figure 3. The principle features of  $\langle G \rangle$  are now discussed for each season.

[16] During MAM, the E-Asian airmass spreads primarily eastward over the Pacific and produces the largest burdens over N America. The transport southwest to SE Asia seen for all the other seasons is nearly absent for MAM.  $\Omega$  air is efficiently exported over the Pacific and reaches the upper troposphere after just a day or two. After one week since last  $\Omega$  contact, the largest concentrations are still seen in the lower troposphere west of the dateline, but upper-level  $\Omega$  air has advanced more quickly, producing eastward sloping contours. The first  $\Omega$  air arriving over western N America does so aloft (see also below). After 8–10 days the bulk of  $\Omega$  air lies in the mid troposphere. The meridionally averaged center of the mid-tropospheric  $\Omega$ -air mass then subsides toward the surface over the subtropical Pacific High during the next several days (see also below). Another subsidence center appears in the meridional average at longitudes  $\sim 30$ – $60^\circ$ W after  $\sim 3$  weeks (not shown).

[17] A useful measure of how successful the flow is in removing boundary-layer air from the source region is the global atmospheric burden of  $\Omega$  air per transit-time interval. Air that does not escape the boundary layer and makes contact again with  $\Omega$  is removed from consideration by the boundary conditions and does not contribute to the  $\Omega$ -air of longer transit times. The NH-average burdens of E-Asian air that had its last  $\Omega$  contact between 2 and 3 days ago (negligible leakage into the SH) are 9.0, 13.1, 12.1, and 9.3 kg m $^{-2}$  for DJF, MAM, JJA, and SON, respectively, showing more efficient removal during MAM and JJA than during SON and DJF.

[18] DJF transport is qualitatively similar to that of MAM. However, some of the lower-level  $\Omega$  air, which for MAM spreads over the western Pacific, is diverted to SE Asia (see also below). During DJF,  $\Omega$  air is least successful in escaping the contact patch, so that, for example, 7-day NH DJF burdens are reduced by  $\sim 20\%$  from their corresponding JJA values. The upper troposphere is reached only after  $\sim 4$  days. The ascent to the mid troposphere is followed by descent after  $\sim 7$  days since last  $\Omega$  contact. As  $\Omega$  air propagates eastward it also travels northward during ascent. Meridional and isentropic cross sections (not shown) suggest that the sloping ascent, subsequent mixing and descent are broadly consistent with quasi-isentropic transport (see also the cross-sections below). This also occurs during MAM, but is less pronounced.

[19] For JJA, convection efficiently injects  $\Omega$  air into the upper troposphere, resulting in global burdens nearly as high as for MAM. However, JJA transport occurs primarily in the upper atmosphere, and involves not only mid-latitude westerlies but also subtropical upper-level easterlies which transport a significant fraction of the  $\Omega$ -air aloft across SE

Asia and India to the Middle East. The JJA transport to the Middle East is consistent with the finding by *Li et al.* [2001] that pollutants from SE Asia contribute to the  $O_3$  maximum in the upper troposphere over the Middle East. There is some evidence of subsidence over the eastern Pacific (see also below), but this subsidence is much weaker than for the other seasons.

[20] As expected, SON transport is intermediate between JJA and DJF transport. There is still enough convective activity for rapid access to the upper troposphere, and transport to SE Asia occurs both at low and high levels. Detailed slices through  $G$  reveal that some of the convectively lofted  $\Omega$  air progresses across the Pacific at mid-tropospheric levels at  $\sim 30$ – $40^\circ$ N, while a second branch appears to spread quasi-isentropically, similarly as for DJF. The  $\Omega$ -air mass subsides over the eastern Pacific (see Figure 3), with the two branches merging.

### 3.2. Most Probable Transit Time and Climatological $\Omega$ -Air-Mass Fraction: Surface and Cross-Sections at $124^\circ$ W

[21] A useful transport timescale is provided by the mode of the transit-time pdf, that is, by the “peak time”, the most probable transit time where the pdf has its maximum. Figure 4 shows the peak times of  $\langle G \rangle$  on the lowest model level together with the corresponding average  $\Omega$ -air-mass fraction that had its last contact during 24-hr intervals 7, 14, and 21 days ago. MAM and DJF transport reaches the western N-American surface soonest ( $\sim 12$ – $14$  days after last  $\Omega$  contact). SON transport is a few days slower, and JJA transport to the surface is slowest with a peak time at the western N-American surface of  $\sim 3$  weeks. For all seasons, the surface signature over North America shows a correlation with topography, consistent with the largest  $\Omega$ -air-mass fractions advancing quickly in the mid troposphere. On average, high elevations see  $\Omega$ -air-mass fractions characteristic of the mid troposphere after a transit time of  $\sim 12$  days ( $\sim 16$  days for JJA), while lower elevations see more dilute  $\Omega$ -air-mass fractions after an additional several days.

[22] Surface “pools” of 14-day-old  $\Omega$  air can be seen in Figure 4 for DJF, MAM, and SON in the region of the subtropical Pacific High east of Hawaii. These pools begin to form  $\sim 10$  days after last  $\Omega$  contact, and the effect is most pronounced for DJF. Formation of the pools is dominated by subsidence which counteracts the dilution of  $\Omega$  air propagating near the surface. This is particularly clear when examining the surface–800 mb vertically integrated budget of  $\Omega$  air (not shown). In the region of the pools, the tendency of the slab burden plus the divergence of the slab-integrated horizontal fluxes is positive, implying subsidence from aloft. For MAM, the central N Pacific surface mixing ratios appear to be produced by low-level advection. For JJA, the surface–800 mb budget shows subsidence off the California coast around day 15, which is joined by low-level advection around the NE Pacific rim (with an anticyclonic sense). The presence of these pools (also visible in Figure 3) suggests that for transit times beyond  $\sim 2$  weeks, both low-level advection from the pools and downward transport from aloft bring older  $\Omega$  air to N America. For particular springtime transport events, *Heald et al.* [2003] and *Hudman et al.* [2004] find subsidence over the Pacific



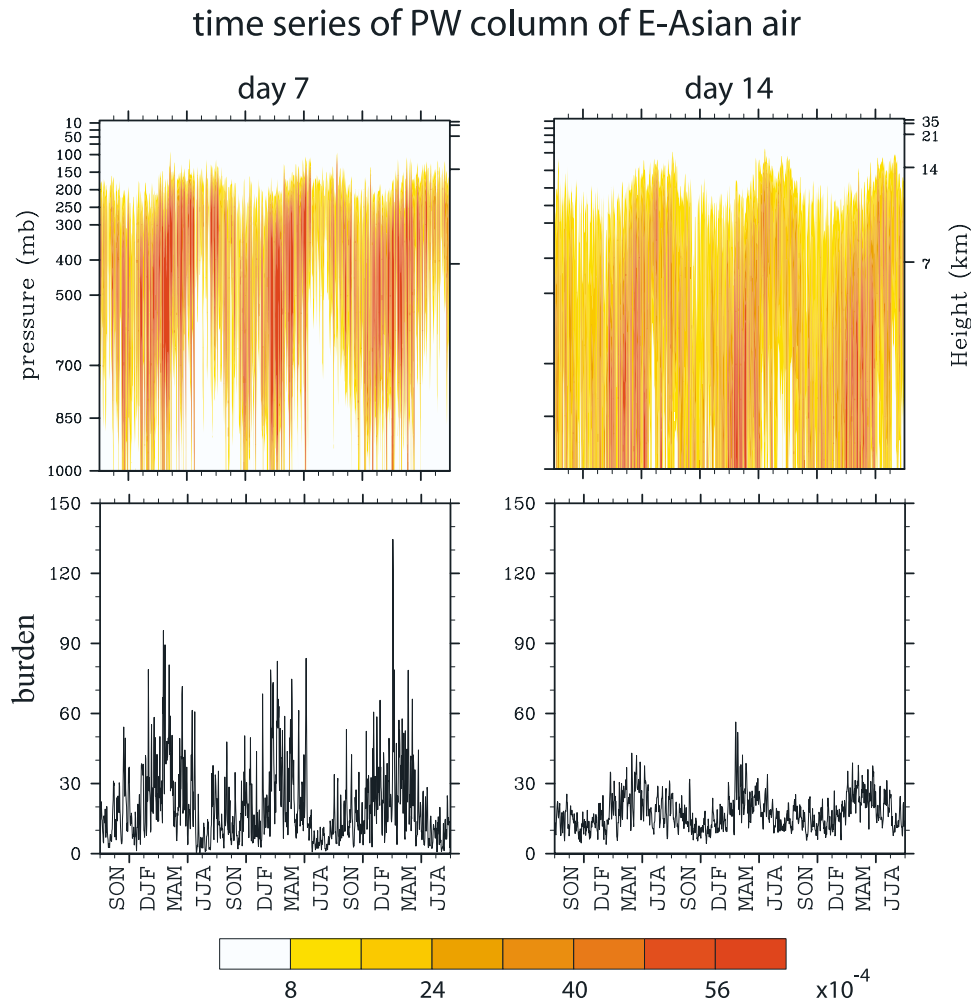


**Figure 6.** Top panels: The vertical distribution (linear in pressure) of the daily PW-averaged column of air that had its last contact with the E-Asian contact region during the 24-hour periods 7 and 14 days ago as indicated for the full 3-year study period. Bottom panels: The corresponding PW-averaged burdens of E-Asian air in  $\text{kg/m}^2$ .

to be associated with  $\text{O}_3$  production via peroxyacetylnitrate decomposition.

[23] To summarize the vertical structure of the most probable transit times, Figure 5 shows meridional cross sections of the peak time at  $124^\circ\text{W}$  together with the mean E-Asian air-mass fraction  $\langle \mathcal{G} \rangle$  that had its last contact during the 24-hr periods 7 and 14 days ago. The northward sloping contours of  $\mathcal{G}$  apparent at 14 days for DJF, MAM, and to a lesser extent for SON, are consistent with quasi-isentropic mixing. MAM has the highest E-Asian air-mass fractions. The fastest peak times of  $\sim 6$  days occur in the upper troposphere, while the most probable transit times to the surface are about a week longer. DJF E-Asian air-mass fractions have similar patterns, but reduced magnitude, and upper tropospheric peak times are 1–2 days longer. JJA air-mass fractions are located primarily in the mid-to-upper troposphere. SON has peak transport times that are very similar to those for MAM, but the associated mass fractions are smaller.

[24] Although the focus of this paper is long-range transport from E Asia to N America, transport to other populated regions is also evident. In particular, there is

pronounced transport to densely populated SE Asia. Peak transport times to the region are  $\sim 2$ –3 days for all seasons, except MAM which is dominated by transpacific transport. JJA transport to SE Asia is via the upper troposphere, while SON and DJF transport is close to the surface, with SON retaining some of the convective upper-level signature of JJA. The easterly transport of E-Asian air during JJA reaches NE Africa and the eastern Mediterranean in the uppermost troposphere with 6 to 7-day peak transit times. Mid-latitude westerly transport brings E-Asian air to Europe during all seasons after it has passed over N America. The largest E-Asian air-mass fractions over Europe occur during MAM in the upper troposphere, where peak transit times range from 12 to 16 days at longitude 0, depending on altitude and latitude.

#### 4. Variability of $\Omega$ Air Over Western North America

[25] To analyze the variability of transport from E Asia, we focus here on the receptor region of western N America as defined in Figure 1 (the “Pacific West” region, PW).

## E-Asian air burden over the PW region

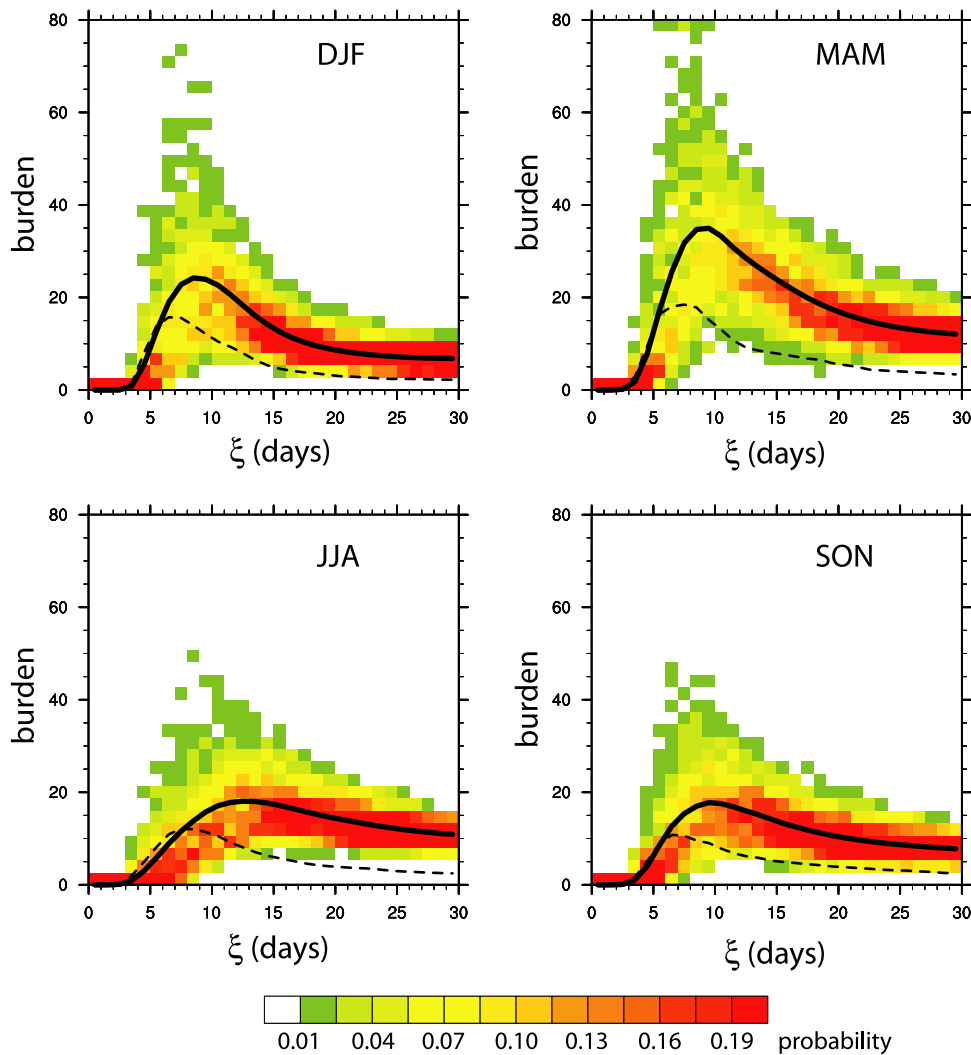


**Figure 7.** Solid line: The seasonal-mean, vertically integrated transit-time pdf, which is the burden of E-Asian air that had its last  $\Omega$  contact during a 24-hour interval  $\xi$  days ago, in  $\text{kg m}^{-2}$ . Dashed line: The corresponding standard deviation. Color shading: Normalized histograms of the burden of E-Asian air in each 24-hour transit-time interval, expressed as the probability of finding the burden in a given pixel. For MAM, the top row of pixels represents the cumulative probability of the burden exceeding  $77.3 \text{ kg m}^{-2}$ .

This region is larger than that used in *Holzer et al.* [2003], so that transport to all of mid-latitude western N America is captured.

#### 4.1. General Character of the Variability

[26] Figure 6 shows PW-area-averaged E-Asian air that had its last  $\Omega$  contact during the 24-hr periods 7 and 14 days ago as a function of (field) time for the entire 3-year period, Sep. 1998–Aug. 2001. The  $\Omega$ -air fraction is highly variable from day to day and displays a pronounced seasonal cycle (as does the tropopause height, also evident in the figure). Consistent with the climatological averages, “young” ( $\sim 7$ -day transit times)  $\Omega$  air reaches the surface primarily during DJF and MAM, while the JJA signal is reduced throughout the column. Thus, the time series of the burden of 7-day old air has its minimum during JJA and its maximum

during MAM. After 14 days since last contact, the  $\Omega$  air reaches the surface during all seasons, eliminating the JJA minimum and producing a seasonal cycle of the burden that is still peaked during MAM but has its minimum late SON to early DJF. While the amplitude of the seasonal cycle decreases with increasing transit time, the phase and shape of the cycle do not change appreciably after  $\sim 3$  weeks (not shown).

[27] The variability of PW-averaged  $\Omega$  air depends strongly on the time since last  $\Omega$  contact. For example, for transit times of  $\sim 2$  days, no  $\Omega$  air reaches N America, that is, zero signal with zero variability. On the other hand, there is large weather-driven variability when synoptic-scale flow begins to sweep filamented E-Asian air across the PW region. For longer transit times, increasingly homogenized  $\Omega$  air results in ever decreasing variability in the tail of  $\mathcal{G}$ .

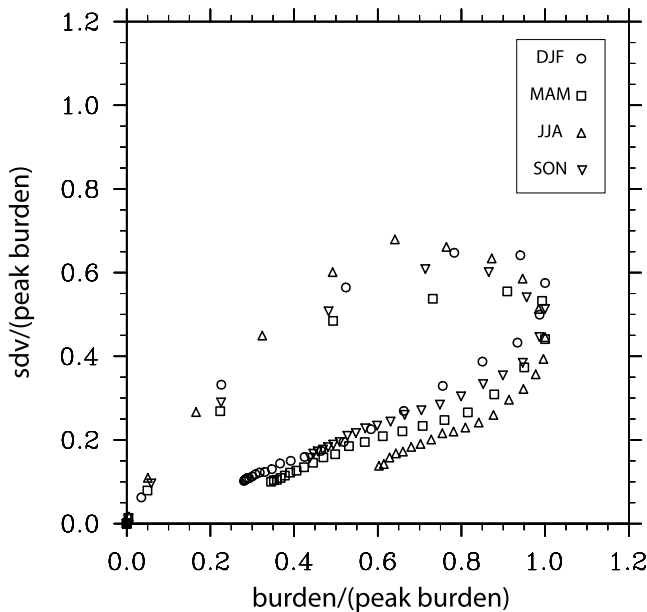


**Figure 8.** The standard deviation of the PW burden of  $\Omega$  air for each 24-hour transit-time interval of Figure 7 plotted versus the corresponding mean burden. For each season, standard deviation and mean have been normalized by the peak value of the seasonal mean burden.

[28] The variability of the PW-averaged E-Asian air already evident in Figure 6 is quantified in detail in Figure 7, which shows the 3-year seasonal mean burdens (solid curve), as well as the probability distribution of the burden (color shading), for each 24-hr transit-time interval as a function of transit time. The probability distribution, which may be thought of as the day-to-day scatter in the transit-time pdf, is obtained by binning the daily burdens in each 24-hr transit-time interval. The resulting histograms have been normalized for each transit-time interval and the black curve is the corresponding mean value. The value of one standard deviation from the mean is shown by the dashed curve. For all seasons, the variability is zero for the first few days, then rapidly increases to peak at a transit time of  $\sim 7$  days, when the burden has approximately its sharpest increase. For longer transit times,  $\Omega$  air becomes increasingly homogenized, making it increasingly less likely for the flow to generate new gradients and local variability. Note that the distribution of  $\Omega$  air in a given transit-time interval is, at least for the first two weeks of transit time, highly asymmetric around the mean and skewed toward large positive excursions. The most probable burdens fall well below the seasonal mean burden, indicating that the seasonal mean is heavily influenced by outliers of unusually high E-Asian burdens. Consequently, the mean and variance do not give a full description of the fluctuations for transit times less than  $\sim 2$  weeks.

[29] Remarkably, the variability of  $\mathcal{G}$  has the same generic structure for all seasons, although the amplitudes of the mean and standard deviation show definite seasonality. To underscore the similarities, Figure 8 shows the standard deviation of the burden plotted versus its mean for each 24-hr transit-time interval of Figure 7, with both standard

deviation and mean expressed as fractions of the peak burden. The loci of points traced out with increasing transit time collapse to a nearly universal curve for all seasons. Roughly, the standard deviation is equal to the mean while fluctuations are growing, and equal to a third of the mean in the decay phase of the ensemble-mean burden. The peak standard deviation is roughly 60% of the peak burden. The nearly universal relationship seen in Figure 8 is an intriguing result that allows one to predict the transit-time partitioned variability from only a knowledge of the corresponding mean. This suggests that a generic physical mechanism is driving the variability. We plan to investigate further with suitable idealized models in a future study.

[30] We also investigated the variability of  $\mathcal{G}$  integrated over three separate layers: surface–700 mb, 700–400 mb, 400 mb–top of atmosphere (not shown). The character of the variability of each layer is similar to that displayed for the entire column. The standard deviation scales with the mean layer-integrated  $\mathcal{G}$ , which does have vertical structure (e.g., Figures 3 and 5).

#### 4.2. Probability of $\Omega$ -Air Exceeding a Given Threshold Value

[31] Holzer *et al.* [2003] analyzed springtime transport with the aim of identifying and quantifying transport “events”, that is, calendar days when the  $\Omega$ -air fraction was above the 90th percentile of its sample distribution. Here we ask the related, but more general, question of what the probability is that potentially polluted E-Asian air exceeds a specified threshold as a function of that threshold.

[32] We focus on the PW-averaged  $\Omega$ -air burden of age  $\tau$  days or less,  $\tilde{\chi}_{PW}(t; \tau) \equiv \int_0^\tau d\xi [\tilde{\mathcal{G}}(\mathbf{r}, t|t - \xi)]_{PW}$ . Note that  $\tilde{\chi}_{PW}$  is similar to the burden of the air-mass fraction  $f$  carrying a chemical species of constant decay time  $\tau$  (see section 2), but with the exponential decay replaced with a step-function decay. The variability of  $\tilde{\chi}_{PW}$  represents the aggregate of the variability of each 24-hr transit-time interval up to  $\tau$  days, allowing us to capture the effect of averaging the fluctuations of  $\mathcal{G}$ . The larger  $\tau$ , the more fluctuations get averaged, reducing the variability of  $\tilde{\chi}_{PW}$ .

[33] Figure 9 shows  $\mathcal{N}(\tilde{\chi}_*, \tau)$ , the fraction of days of a given season for which  $\tilde{\chi}_{PW}(t; \tau)$  exceeds the threshold value  $\tilde{\chi}_*$ . [This statistic is efficiently computed by simply sorting the daily PW-averaged values of  $\tilde{\chi}_{PW}(t; \tau)$  for a given season and all three years and plotting normalized rank in the sorted list versus  $\tilde{\chi}_*$ .] Note that the seasonal median value of  $\tilde{\chi}_{PW}$  corresponds to the value of  $\tilde{\chi}_*$  where the curves intersect the line  $\mathcal{N} = 50\%$ . If the PW burden is measured in units of the annual mean (left-hand panels of Figure 9), it is apparent that MAM has the largest seasonal mean and median  $\Omega$  burdens. The fraction of days for which a given threshold is exceeded is readily read off the figure. For example, the  $\Omega$ -air burden of age 7 days or less exceeds twice (three times) its annual mean for  $\sim 30\%$  ( $\sim 14\%$ ) of MAM days.

[34] Consistent with the scaling seen in Figure 8, if the daily PW burdens are measured relative to their seasonal means, the variability is very similar for all seasons (right-hand panels of Figure 9). For 7-day old or less  $\Omega$  air ( $\tau = 7$  days),  $\sim 12\%$  of the days exceed twice the seasonal mean.

Percentage of days,  $\mathcal{N}$ , for which the PW-averaged  
E-Asian air burden of age  $\tau$  days or less exceeds  $\tilde{\chi}_*$

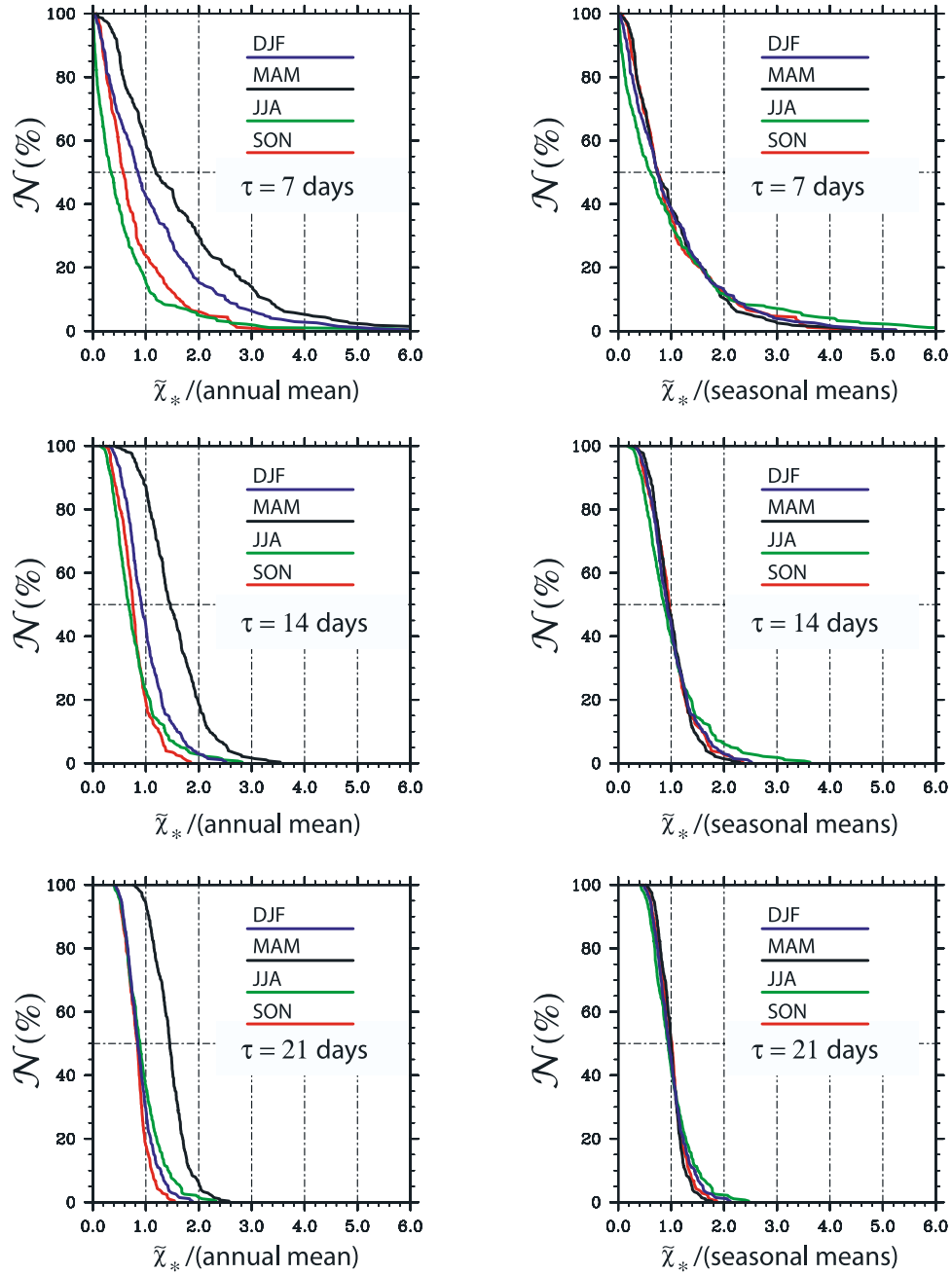


**Figure 9.** Cumulative probability distributions of the PW-averaged E-Asian air-mass burden of age  $\tau$  days or less,  $\tilde{\chi}_{PW}(t, \tau)$ , expressed as the percentage of days,  $\mathcal{N}$ , for which  $\tilde{\chi}_{PW}(t, \tau)$  exceeds  $\tilde{\chi}_*$  as a function of  $\tilde{\chi}_*$ . For the left-hand panels  $\tilde{\chi}_*$  is expressed in units of the annual mean, and for the right-hand panels  $\tilde{\chi}_*$  has been expressed in units of the seasonal means.

Note that the median values of  $\tilde{\chi}_{PW}$  are at least 20% lower than the means for  $\tau = 7$  days, again pointing to the highly skewed nature of the fluctuations. As  $\tau$  is increased, the medians converge to their corresponding means [that is, the curves pass through the point (1, 50%)] as fluctuations

become more symmetric about the mean. The means and standard deviations of  $\tilde{\chi}_{PW}$  for  $\tau = 7, 14, 21$ , and 28 days are summarized in Table 1. To give some indication of the vertical structure of  $\mathcal{N}$ , we collect in Table 2 the number of days for which the surface–700 mb, 700–400 mb, and



**Table 1.** Means and Standard Deviations of the PW Burden of E-Asian Air of Age  $\tau$  or Less<sup>a</sup>

		$\tau = 7$	$\tau = 14$	$\tau = 21$	$\tau = 28$ days
	annual mean	33.	178.	277.	348.
DJF	mean/ann. mean	1.14	1.00	0.89	0.85
MAM	mean/ann. mean	1.62	1.54	1.45	1.40
JJA	mean/ann. mean	0.57	0.78	0.94	1.03
SON	mean/ann. mean	0.76	0.78	0.83	0.86
DJF	sdv/mean	0.90	0.42	0.31	0.26
MAM	sdv/mean	0.77	0.35	0.22	0.18
JJA	sdv/mean	1.33	0.58	0.37	0.29
SON	sdv/mean	0.84	0.40	0.26	0.21

<sup>a</sup>The annual means are given in units of kg/m<sup>2</sup>, the seasonal means in units of the annual mean, and the standard deviations in units of the seasonal means.

400 mb–top layer burdens exceed 1.5 times their seasonal means. (This threshold was chosen to ensure that  $\mathcal{N}$  is nonzero for our finite data set even for  $\tau = 21$  days.)

[35] To quantify the persistence of fluctuations in  $\tilde{\chi}_{PW}(t; \tau)$ , we calculated its autocorrelation function. A rough timescale for the persistence is given by the first zero crossing of the autocorrelation. For all seasons this is  $\sim 4$  days for  $\tau = 7$  days and increases to  $\sim 5$ –6 days for SON, JJA, and MAM (not for DJF) as  $\tau$  is increased to 21 days. This timescale is consistent with synoptic-scale weather systems driving the observed variability in  $\tilde{\chi}_{PW}$ .

## 5. Flow Structures Associated With Effective and Ineffective Transpacific Transport

### 5.1. Lagged Event and Nonevent Composites

[36] In *Holzer et al.* [2003], the time series of  $\Omega$  air in a given transit-time interval was regressed onto the local winds with a lag of  $\tau$  days to identify the perturbations from the mean state that led to enhanced  $\Omega$  air burdens over the Pacific Northwest. Here we take a related approach to identify the flow structures that lead to particularly high PW  $\Omega$ -air burdens and to contrast those to flow structures that are ineffective in enhancing the PW  $\Omega$ -air burden. Instead of forming the regression with the entire time series of the PW  $\Omega$ -air column, we form a composite of the flow  $\tau$  days earlier only if the  $\Omega$ -air burden lies either above or below a threshold value, with each member of the composite weighted by the  $\Omega$ -air burden.

[37] More precisely, we form the time series,  $\psi(t; \xi) \equiv [\tilde{G}(\mathbf{r}, t|\Omega, t - \xi)]_{PW}$  for fixed transit time  $\xi = t - t'$ . The time series  $\psi(t; \xi)$  is the PW-averaged burden of  $\Omega$  air at time  $t$  that had its last  $\Omega$  contact during the 24-hr period  $\xi$  days ago. To calculate correlations or composites between  $\psi$  and other fields, we use  $\hat{\psi}$  obtained from  $\psi$  by (1) subtracting a quadratic fit to the time series for each season to remove the low-frequency contribution of the seasonal cycle, followed by (2) “standardization”, which removes the mean and divides by the variance. Weighted composites are then essentially regressions with  $\psi$  zeroed when it does not satisfy the threshold criterion. Thus, we form an “event composite” with  $\hat{\psi}^+(t; \xi, \psi_0^+) \equiv \hat{\psi}(t; \xi)$  if  $\hat{\psi}(t; \xi) \geq \psi_0^+$  and  $\hat{\psi}^-(t; \xi, \psi_0^-) \equiv 0$  otherwise, and a “nonevent composite” with  $\hat{\psi}^-(t; \xi, \psi_0^-) \equiv \hat{\psi}(t; \xi)$  if  $\hat{\psi}(t; \xi) < \psi_0^-$  and  $\hat{\psi}^+(t; \xi, \psi_0^+) \equiv 0$

otherwise. Weighted composites, lagged by  $\tau$  days, of a field  $X$  are then simply obtained as

$$\langle X \rangle^\pm(\mathbf{r}; \xi, \tau, \psi_0^\pm) \equiv \langle X(\mathbf{r}, t - \tau) \hat{\psi}^\pm(t; \xi, \psi_0^\pm) \rangle / \langle \hat{\psi}^\pm(t; \xi, \psi_0^\pm) \rangle, \quad (2)$$

where the angle brackets denote an average over  $t$ . Thus, the composite  $\langle X \rangle^+$  is a weighted average of those  $X$  for which the standardized PW burden,  $\hat{\psi}$ , satisfies the condition  $\hat{\psi} \geq \psi_0^+$ , while the composite  $\langle X \rangle^-$  is a weighted average of those  $X$  for which  $\hat{\psi} < \psi_0^-$ . In this sense, the composites are conditional averages, conditioned on  $\hat{\psi}$ .

[38] To compute composites, we conditioned on the PW burden of 7-day-old E-Asian air (that is,  $\xi = 7$  days). One could in principle use the time series of the PW-averaged burden for any value of  $\xi$ , but we choose 7 days to capture the maximum variability (see Figure 7). The corresponding composites capture flow structures that lead to the most direct transport of coherent E-Asian air masses to the PW region. If one conditions on the time series of significantly older air, the resulting time-lagged composites are more difficult to interpret because of the greater number and circuitry of pathways by which advective-diffusive flow brings older air to the PW.

[39] For event composites, we choose a threshold of  $\psi_0^+ = 1$  (everything above one standard deviation) and for nonevent composites, a threshold of  $\psi_0^- = 0$  (everything below the mean). For event composites this averages 14%, 14%, 11%, and 14% of the days for DJF, MAM, JJA, and SON, respectively. The corresponding percentages for nonevent composites are 61%, 55%, 59%, and 59%. The qualitative patterns of the composites were insensitive to the choice of threshold, with changes as large as plus/minus one standard deviation giving similar results. Computing the composites with equal weights, rather than  $\hat{\psi}$  weights, reduced the amplitude of the patterns but preserved their qualitative character. We attribute this insensitivity to the

**Table 2.** Percentage of Days,  $\mathcal{N}$ , for Which a Threshold of 1.5 Times the Seasonal Mean is Exceeded by the PW-Averaged E-Asian Air Mass Fraction of Age  $\tau$  Days or Less<sup>a</sup>

		$\mathcal{N}, \%$		
		$\tau = 7$	$\tau = 14$	$\tau = 21$ days
DJF	UPR	22.	15.	11.
	MID	22.	13.	11.
	LWR	23.	12.	8.2
MAM	COL	22.	13.	7.5
	UPR	20.	15.	10.
	MID	26.	10.	3.7
JJA	LWR	22.	15.	5.1
	COL	22.	8.5	2.9
	UPR	22.	13.	7.1
SON	MID	17.	18.	13.
	LWR	10.	19.	19.
	COL	21.	14.	10.
	UPR	22.	14.	9.9
	MID	18.	13.	8.3
	LWR	16.	18.	8.8
	COL	21.	12.	4.0

<sup>a</sup>Values are tabulated for layer integrals (UPR: 400 mb – top, MID: 700 mb–400 mb, LWR:  $p_s$  – 700 mb) and for the entire column burden (COL).

event composites at a lag  $\tau=2$  days with  $\xi=7$  days

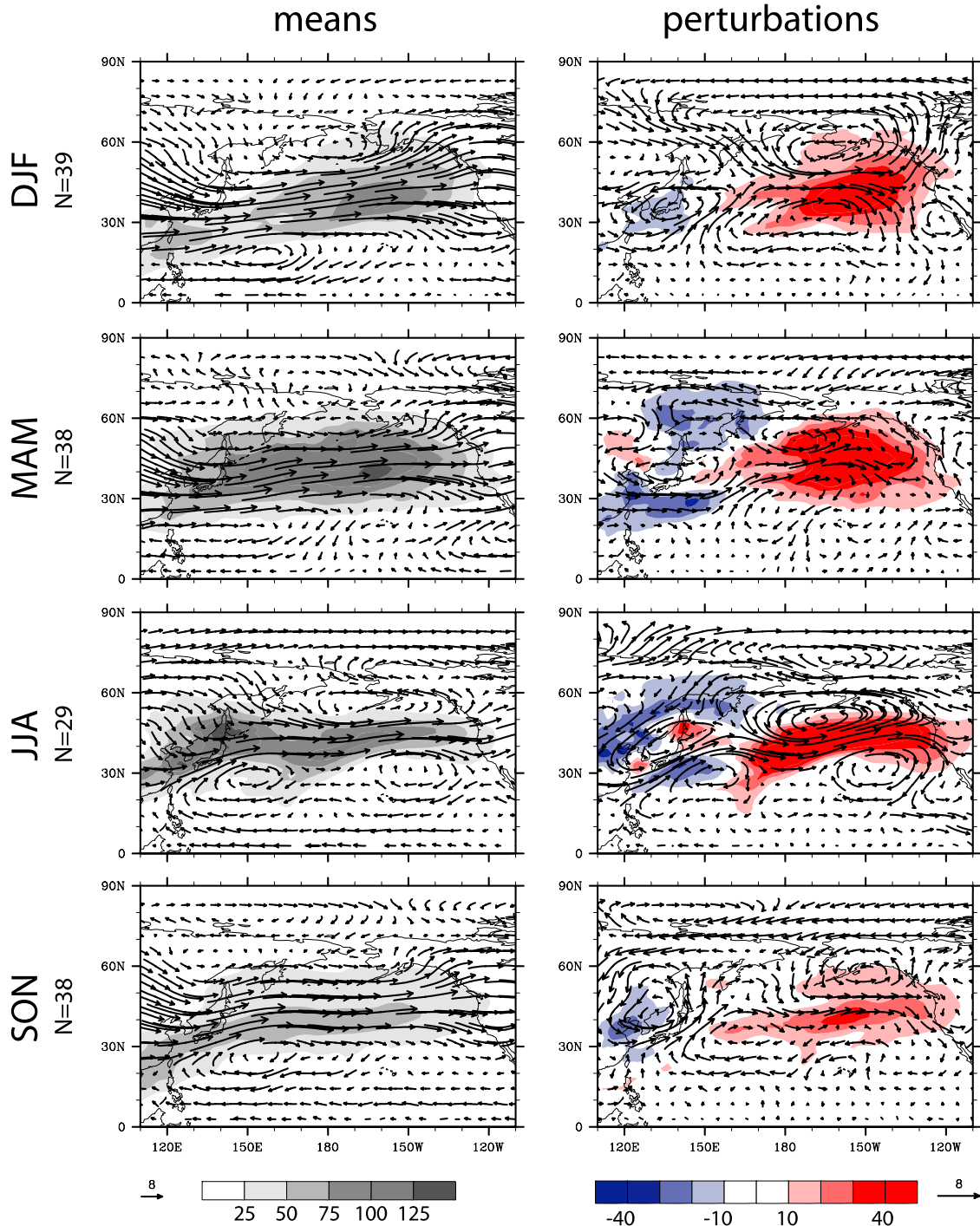


**Figure 10.** Left-hand panels: Event-composites of the 500-mb winds,  $\langle u, v \rangle^+$ , and of the E-Asian air burden,  $\langle \tilde{G} \rangle^+$ , conditioned on the standardized time series of  $\xi = 7$ -day old, PW-averaged  $\Omega$ -air burden falling above one standard deviation ( $\psi_0^+ = 1$ ), and lagged by  $\tau = 2$  days. Right-hand panels: The perturbation fields  $\delta\langle u, v \rangle^+ \equiv \langle u, v \rangle^+ - \langle u, v \rangle$  and  $\delta\langle \tilde{G} \rangle^+ \equiv \langle \tilde{G} \rangle^+ - \langle \tilde{G} \rangle$  obtained by removing the seasonal means. The number of days contributing to the composites is indicated by  $N$ . The composites are shown for each season as indicated. The burden is in units of  $\text{kg m}^{-2}$ ; the vector scale is in  $\text{m/s}$ .

*non-event composites at a lag  $\tau=2$  days with  $\xi=7$  days*

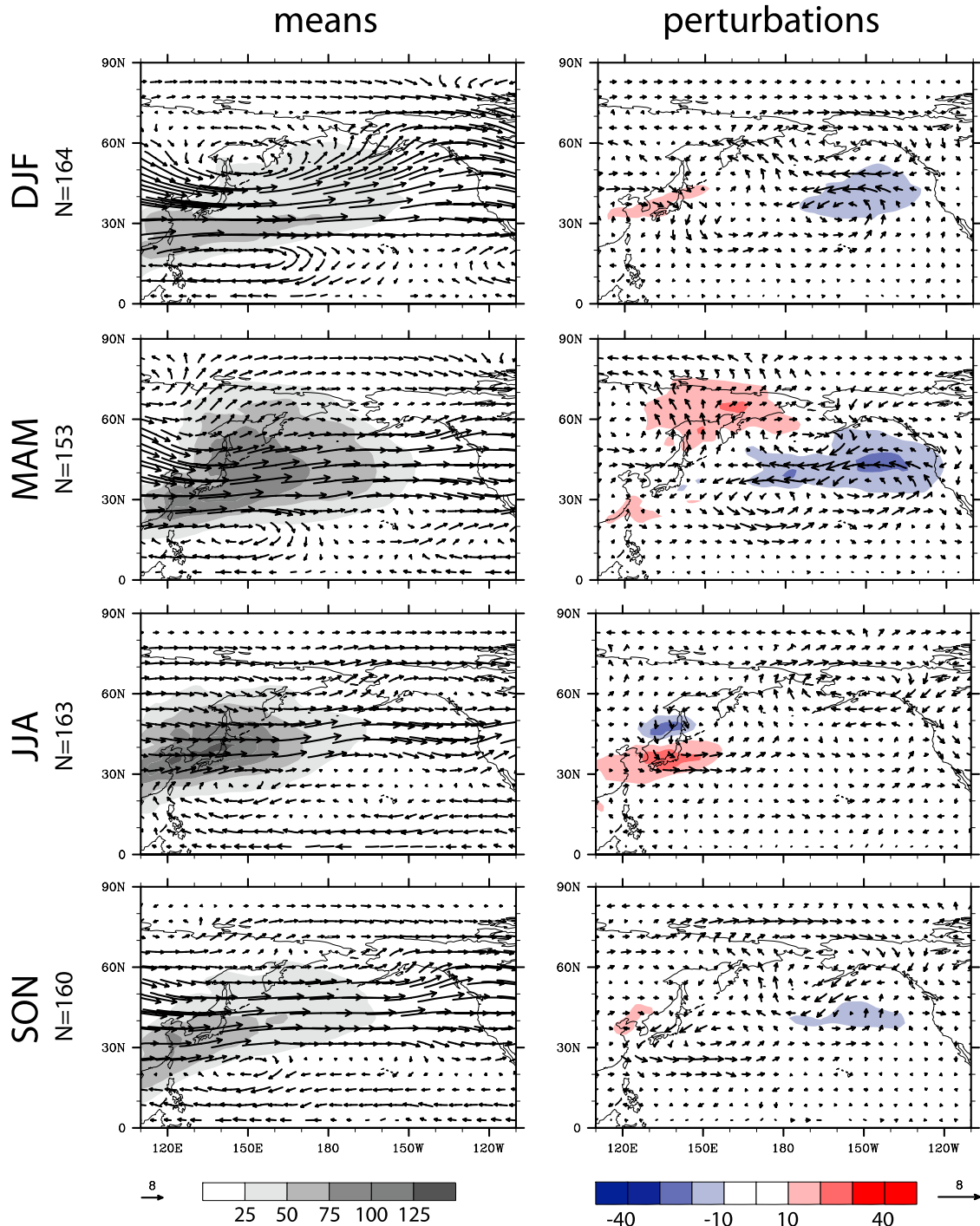


**Figure 11.** As for Figure 10 but for the nonevent composites  $\langle u, v \rangle^-$ , and  $\langle \tilde{G} \rangle^-$ , conditioned on the standardized time series of 7-day old, PW-averaged  $\Omega$ -air burden falling *below* its mean ( $\psi_0^- = 0$ ).

skewed nature of the fluctuations at early transit times (see Figure 7), which also guided our asymmetric choice of thresholds.

[40] It is worth noting that advection by the event-composited winds dominates the mid-troposphere horizontal transport for the subset of realizations satisfying the

event conditioning. Transient eddies within this subset are less important. More precisely, the event-composited advective horizontal fluxes of E-Asian air (not shown),  $\langle u\mathcal{G}, v\mathcal{G} \rangle^+$ , are approximately given by  $\langle u, v \rangle^+ \langle \mathcal{G} \rangle^+$ , with the “eddies”,  $\langle u\mathcal{G}, v\mathcal{G} \rangle^+ - \langle u, v \rangle^+ \langle \mathcal{G} \rangle^+$ , being an order of magnitude smaller.

# perturbation event composite evolution at 500 mb for $\xi = 7$ days

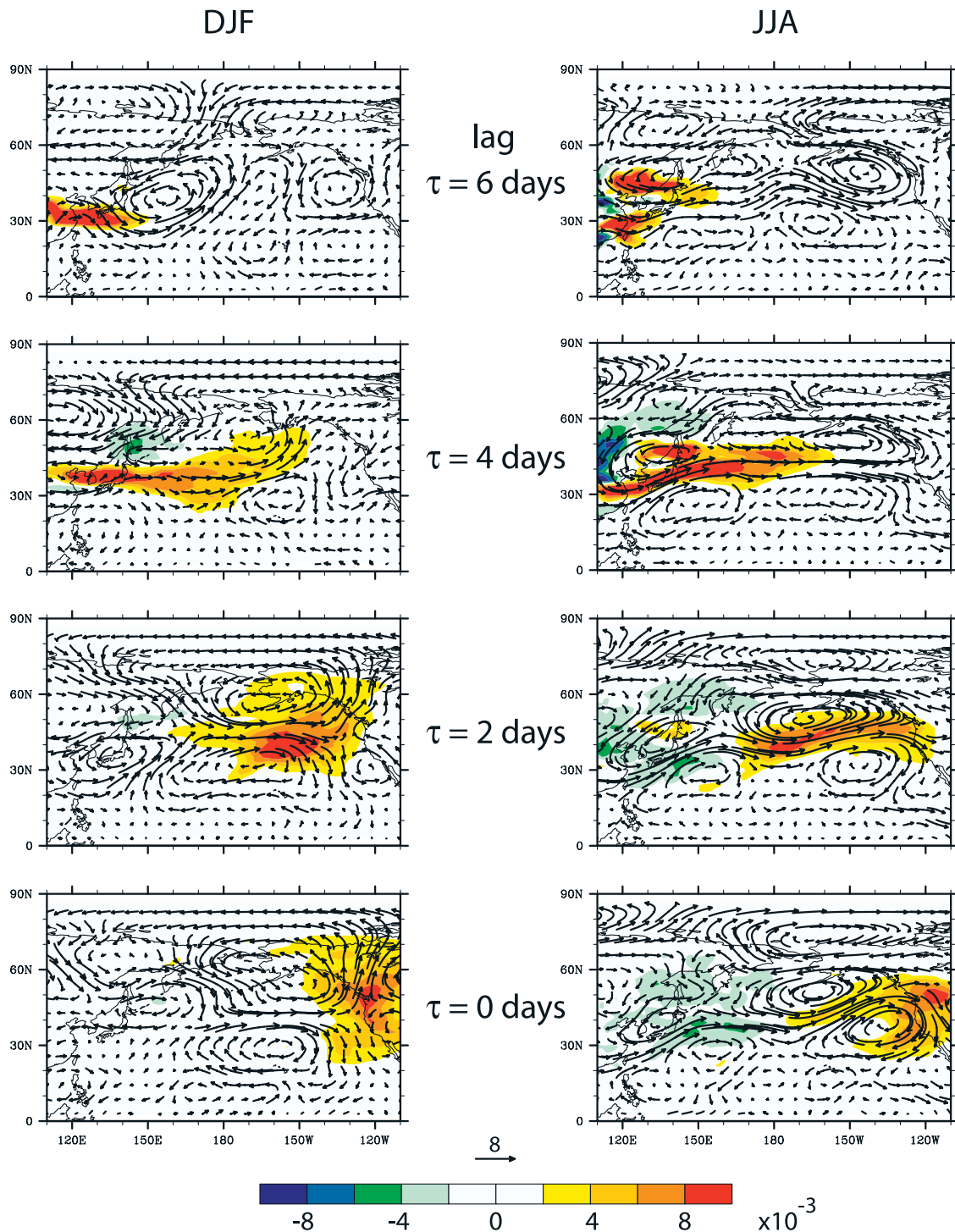


**Figure 12.** Perturbation event-composites of the winds,  $\delta \langle u, v \rangle^+$ , and of the E-Asian air-mass fraction,  $\delta \langle G \rangle^+$ , both at 500 mb, conditioned on the standardized time series of  $\xi = 7$ -day old, PW-averaged  $\Omega$ -air burden falling above one standard deviation ( $\psi_0^+ = 1$ ), and lagged by  $\tau$  days, as indicated for DJF and JJA. The vector scale is in m/s.

[41] The left-hand panels of Figures 10 and 11 show composites of the 500-mb winds and the burden of E-Asian air lagged by  $\tau = 2$  days. The differences between the event and nonevent composites of the 500-mb flow only become

clear in the perturbations,  $\delta \langle u, v \rangle^\pm \equiv \langle u, v \rangle^\pm - \langle u, v \rangle$ , obtained by subtracting out the climatological seasonal-mean 500-mb winds (computed for the same three years). The lagged perturbation winds,  $\delta \langle u, v \rangle^\pm$  are shown together



with the lagged perturbation burdens  $\delta(\tilde{G})^\pm$  in the right-hand panels of the figures.

[42] The event composites (Figure 10) show the average large-scale conditions that lead to high E-Asian air burdens over the PW. Two days prior to large PW burdens of 7-day old E-Asian air, 5-day old E-Asian air is situated off-shore in the heart of strengthened westerly winds (by up to  $\sim 8$  m/s). The wind perturbations have a dipolar structure of synoptic spatial scale with cyclonic (anti-cyclonic) flow to the North (South) of the enhanced E-Asian air mass. This structure of the perturbation winds implies a strain rate aligned so as to shape the E-Asian air into filaments pointed at western N America (see also the discussion on the time evolution, below). The flow structures that emerge from the event composites are qualitatively similar to those seen from lagged regressions in *Holzer et al.* [2003] for a springtime ensemble using a smaller receptor region. The fact that conditioned event composites and unconditioned regressions give similar patterns underscores the highly skewed nature of the fluctuations of  $\tilde{G}$ . The event composites for DJF and JJA show the strongest wind enhancement over their respective mean states. The flow perturbation for MAM is less coherent than for the solstitial seasons, but MAM has the largest event-composite burdens in the eastern Pacific with comparable shaping of the E-Asian air mass as for DJF. The weakest perturbations in the flow and burden are seen in SON.

[43] The nonevent composites contrast sharply with the event composites. Features common to all seasons are that during nonevent days, 5-day old air is on average still in the western Pacific just off Asia, and the wind perturbations show a weakening of the westerly flow over the eastern Pacific, which for DJF and MAM is in amplitude of the same order as the strengthening seen in the event ensemble. Enhanced transport to Siberia and the Arctic can be seen during MAM. JJA shows enhanced local retention of the 5-day old  $\Omega$  burden with a southward shift from the climatological mean.

## 5.2. Evolution of the Event Composites

[44] The evolution of the event composites ( $\xi = 7$  days,  $\psi_0^+ = 1$ ) with decreasing lag,  $\tau$ , is shown in Figure 12 for DJF and JJA (MAM and SON are qualitatively similar, but SON amplitudes are smaller). To emphasize the spatial structure of the fields, we again show the perturbations from the climatological means. In Figure 12, however, we plot the E-Asian air-mass fraction at 500 mb, not its burden, to make it easier to interpret the relationship between mass fraction and flow. Thus, Figure 12 essentially shows the motion of the 500-mb E-Asian air-mass fraction across the Pacific averaged over those cases where it results in high PW burdens. The composites lagged at  $\tau = 6$  days show the situation 1 day after last  $\Omega$  contact, lagged at  $\tau = 4$  days, 3 days after last contact, and so on.

[45] While the detailed evolution of the event-composited  $\Omega$ -air “cloud” is complex, enhanced  $\Omega$ -air mass fractions can be seen to coincide to a good approximation with enhanced winds during the  $\Omega$ -air’s transpacific journey. These wind enhancements generally have a large westerly component, but are far from purely zonal. The average transpacific progression of  $\Omega$  air that will result in large PW burdens can be broadly characterized as follows. First, 1–

2 days since last  $\Omega$  contact, enhanced winds over Korea, the Sea of Japan, and the western Pacific export  $\Omega$  air from the Asian continent. During DJF these wind perturbations are associated with strong cyclonic circulation over the western Pacific, and during JJA with a dipolar structure centered roughly over Japan (cyclonic to the north). Then, 2–4 days since last  $\Omega$  contact, the  $\Omega$  air enters the inflow region of a dipole perturbation roughly centered over the mid-latitude eastern Pacific, which elongates the  $\Omega$  air toward N America and allows it to maintain its coherence. On completion of the transpacific journey, 5–6 days since last  $\Omega$  contact (1–2 days before “landfall” with N America), the  $\Omega$  air leaves the dipole through its outflow region just off the N American west coast. On expulsion from the dipole, gradients broaden as the  $\Omega$  air is dispersed across the PW region. This sequence of events suggests that in order to have large PW burdens of E-Asian air after a 7-day transit time, it is essential that the weather system that efficiently exports air from Asia is suitably phased with a weather system over the eastern Pacific. The eastern Pacific dipole must be in the right place at the right time to receive the Asian air and have its strain-rate field shape and direct this air toward N America. That several baroclinic systems need to cooperate to generate transpacific transport events has also been demonstrated for a particular case by *Cooper et al.* [2004].

[46] To investigate vertical structure, we show in Figure 13 event composites of the NH meridionally averaged  $\Omega$ -air mass fraction at lags of 3 to 0 days. Remarkably, these show an accelerated, exaggerated version of the evolution of the climatological  $\Omega$ -air mass fraction seen in Figure 3 over a two-week period. DJF and MAM show a slanting ascent of  $\Omega$  air into the mid troposphere consistent with this air being carried by warm conveyor belts [e.g., *Stohl*, 2001; *Cooper et al.*, 2004]. JJA shows direct ascent to the upper troposphere characteristic of convection, followed by eastward transport in the upper troposphere. SON is intermediate between JJA and DJF.

[47] For all seasons there is also some low-level eastward propagation. Figure 14 shows the lag-0 event composites of the (7-day old)  $\Omega$ -air mass fraction and corresponding winds at the lowest model level. For DJF and MAM, the event-composited  $\Omega$  air has already spread over the NE Pacific and much of the western N American surface. JJA shows a more coherent surface signal close to the NE Pacific rim; the SON surface signal is relatively weak and diffuse. The composited surface–800 mb burdens (not shown) indicate that for DJF, MAM, and SON subsidence over the subtropical Pacific High is already contributing to the low-level  $\Omega$ -air mass fraction.

[48] We conditioned event composites on a robust signal, namely the entire column burden averaged over the PW receptor region. From an air-quality perspective it is also interesting to investigate the transport that leads to large surface enhancements of E-Asian air. While a detailed analysis of surface events is beyond the scope of this work, we examined composites conditioned on the surface-to-800 mb burden of 7- and 15-day old E-Asian air (not shown). Conditioned on 7-day old air, the composited wind anomalies at 500 mb are qualitatively similar to those seen in Figures 10 and 12, with dipolar structures for DJF and JJA. The corresponding compo-

# event composite evolution of NH meridional averages for $\xi = 7$ days

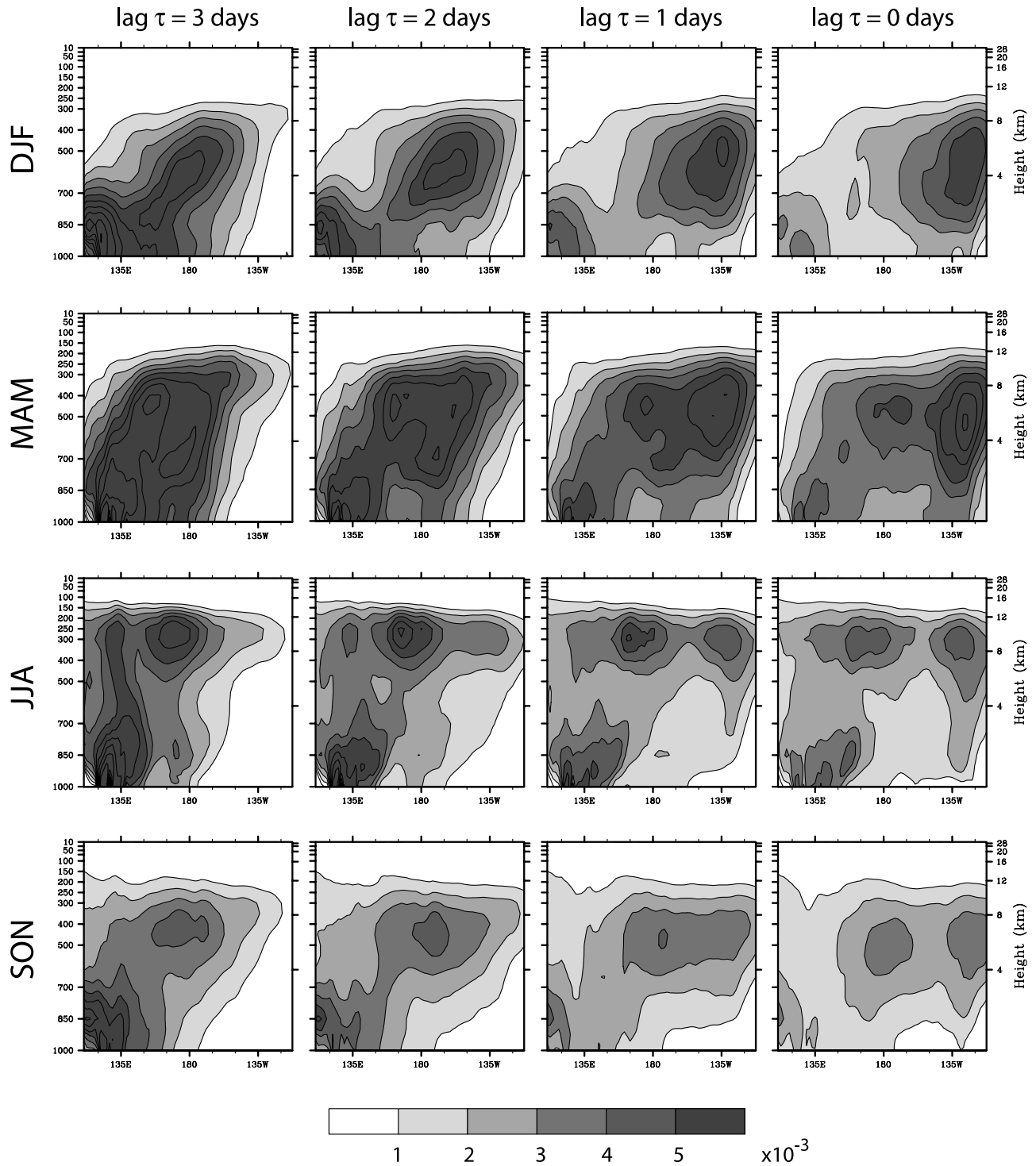


**Figure 13.** Event composites with  $\psi_0^+ = 1$  of the NH meridional average of the E-Asian air-mass fraction conditioned on the standardized time series of  $\xi = 7$ -day old, PW-averaged  $\Omega$ -air burden falling above one standard deviation, and lagged by  $\tau$  days, as indicated. Shown are longitudes 110°E to 110°W, spanning the N Pacific and PW receptor region.

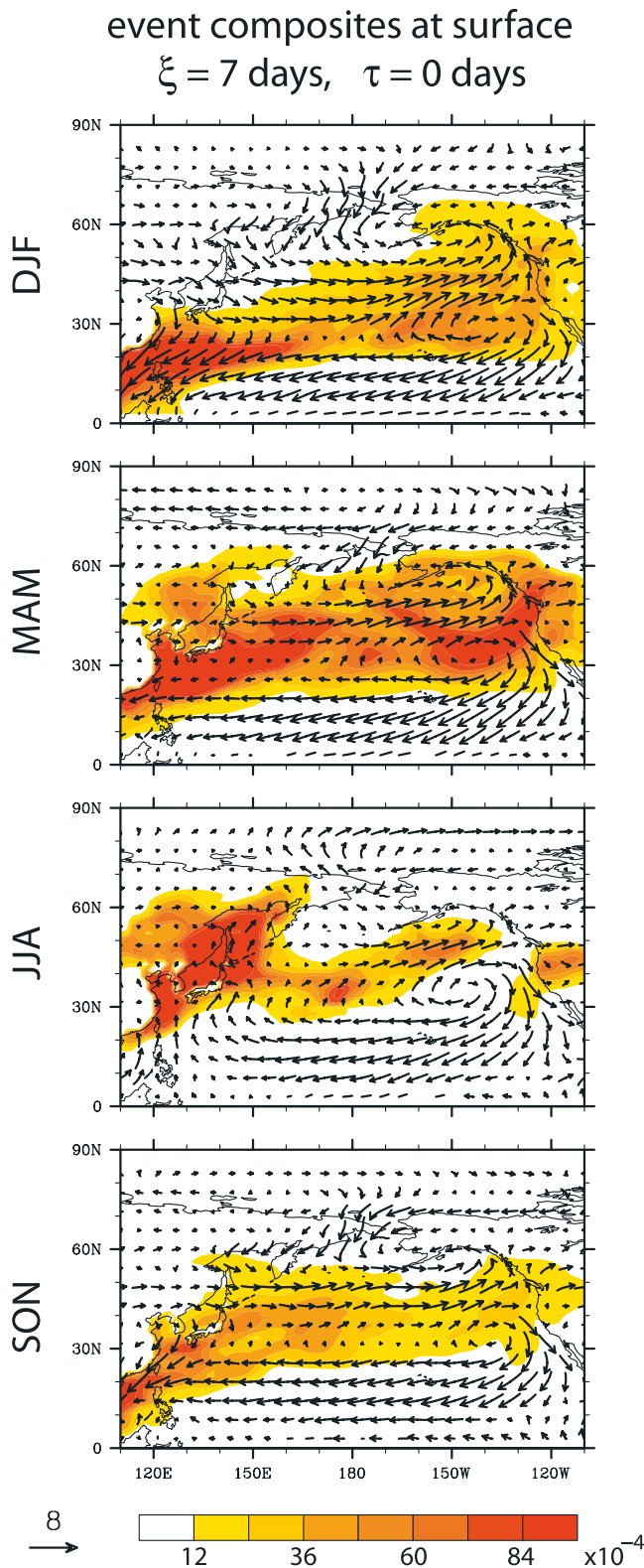


**Figure 14.** Event composites with  $\psi_0^+ = 1$  of the lowest-model-level winds and E-Asian air-mass fraction conditioned on the standardized time series of  $\xi = 7$ -day old, PW-averaged  $\Omega$ -air burden falling above one standard deviation, with zero lag. The vector scale is in m/s.

sites of meridional averages are qualitatively similar to those of Figure 13, except for DJF, MAM, and SON the mid tropospheric centre of E-Asian air shows modest downward extension. Only 9 events contribute to the corresponding JJA composite with a suggestion of more low-level transport than is seen in Figure 13. Conditioned on 15-day old air, the composited meridional averages for DJF, MAM, and SON, show the E-Asian air descending to the surface at  $\sim 140^\circ\text{W}$  4–5 days before landfall, followed by horizontal spreading and dilution. This low-level transport of older air following subsidence corroborates the formation of the Pacific surface pools seen in the climatological averages of section 3.

### 5.3. Surface-Pressure Correlations

[49] The enhanced westerly flow over the NE Pacific seen in the event composites suggests a corresponding surface signature of enhanced meridional pressure gradients with a strengthened Pacific High and deepened Aleutian Low. Figure 15 shows the correlations between the PW-averaged burden of  $\Omega$  air aged 14 days or less (approximately the time scales that would be convolved into an  $\text{O}_3$  burden) and the local surface pressure,  $p_s$ , 2 days earlier computed with the seasonal data of all three years. If these correlations are decomposed into contributions from two-day transit-time intervals (not shown), the contribution from the interval centered around  $\sim 7$  days dominates, as expected from the variability seen in Figure 7. Since our focus here is daily variability, low-frequency seasonal trends in both the time series of PW burden and in the local values of  $p_s$  were removed using a quadratic fit. (If the trend is not removed, the correlations are stronger, suggesting seasonal trends in the burden tend to track seasonal trends in  $p_s$ .) As expected from the composites, the correlations show modest negative correlations over Alaska and modest positive correlations over the subtropical Pacific (the latter are weak for JJA). As the lag is increased from 2 days (not shown), the correlation “bull’s eyes” move west toward Asia and decrease in amplitude, consistent with the flow perturbations of Figure 12.

[50] The lag-2-day correlation patterns suggest forming an index based on the surface pressure difference between Hawaii and Alaska from which the PW E-Asian burden might be statistically forecast. Sea-level-pressure indices have been useful for  $\text{O}_3$  correlations [Liu *et al.*, 2005] and for CO correlations [Liang *et al.*, 2005]. We calculated correlations between the seasonally detrended PW  $\Omega$ -air burden of age 14 days or less and the detrended daily-average Honolulu–Anchorage  $p_s$  difference 2 days earlier. For greater robustness, we also used the difference between the area-averaged  $p_s$  for the regions  $16\text{--}30^\circ\text{N} \times 147\text{--}160^\circ\text{W}$  and  $55\text{--}70^\circ\text{N} \times 147\text{--}160^\circ\text{W}$ . Note that while Figure 15 shows that Honolulu and Anchorage are not for all seasons both in regions of significant local lag-2 correlation, only one of them needs to be well correlated to give a good correlation with the Honolulu–Anchorage pressure difference. The correlation coefficients for individual seasons, and for the three years of seasons combined, are collected in Table 3. Although the correlations with the area averaged index are slightly higher, the results show only very modest correlations when computed using the

correlation at a lag of 2 days between surface pressure and  
PW-averaged E-Asian air of age 14 days or less

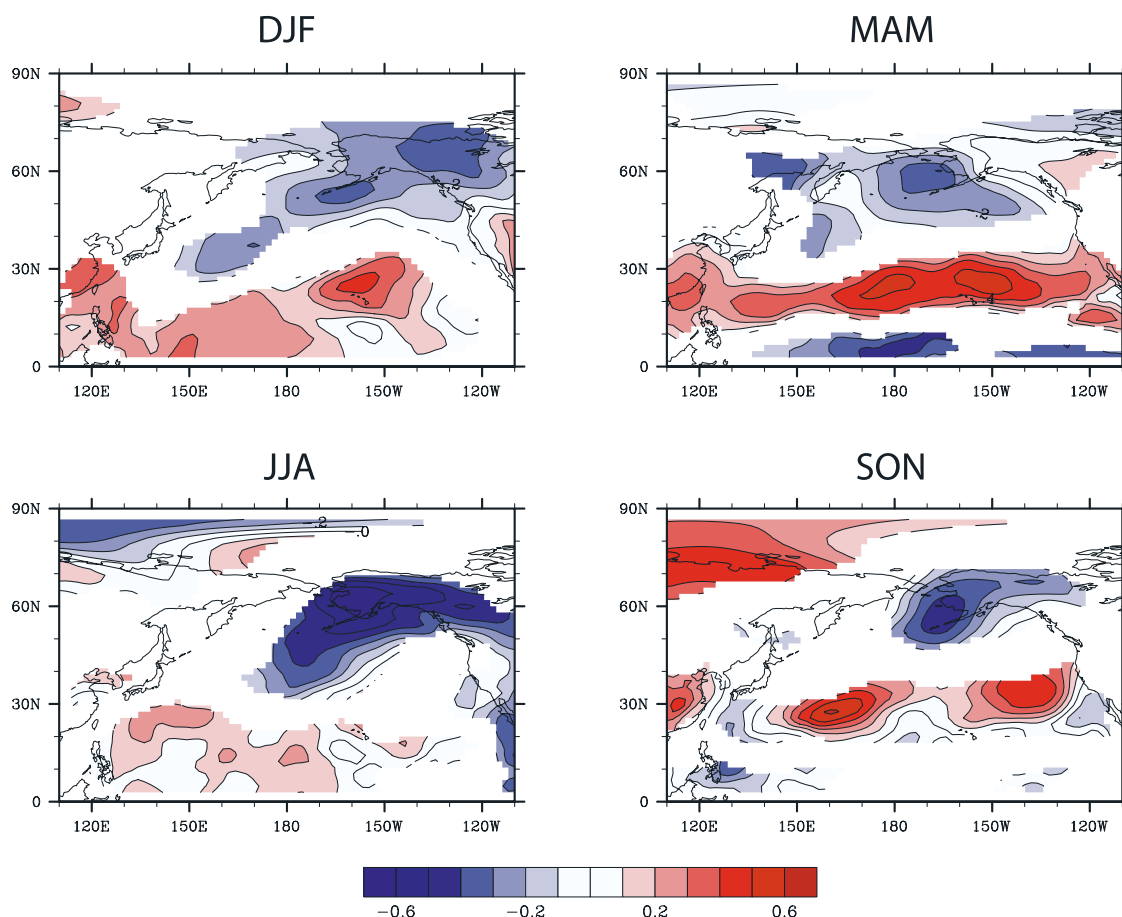


**Figure 15.** Pearson's correlation coefficient,  $r$ , computed between the detrended time series of the PW burden of E-Asian air of age 14 days or less and the detrended time series of the local surface pressure lagged by 2 days for the seasons indicated. Correlations insignificant at the 5% threshold have been masked out.

data for all three years. The correlation for individual seasons can be as high as 0.6.

## 6. Summary and Conclusions

[51] The aim of this study has been (1) to establish the climate of transport from the industrialized E-Asian surface for all seasons of the year, extending the work of Holzer *et al.* [2003], and (2) to quantify the day-to-day variability of transpacific transport in terms of its dependence on transit time and season. We have used a tracer-independent transport diagnostic, the transit-time pdf, which is the air-mass fraction that had its last contact with a specified surface patch in a given time interval. The transit-time pdf allowed us to isolate the role of transport from other factors determining the concentration of chemical species, such as photochemistry and variability in emissions. Diagnosing transport with trace species such as  $O_3$  or CO leads to ambiguity because of the interplay between transport time-scales and chemical evolution involving uncertain OH

fields. Using MATCH driven with NCEP reanalysis data, we have calculated the air-mass fraction that had its last contact with the E-Asian  $\Omega$  patch of Figure 1 during any given day of the three-year period Sep. 1998 to Aug. 2001.

**Table 3.** Pearson's Correlation Coefficient,  $r$ , Computed Between the Detrended Time Series of Daily Averages of the PW Burden of E-Asian Air of Age 14 Days or Less and a Detrended Pressure Index Lagged by 2 Days<sup>a</sup>

	All Years	Year 1	Year 2	Year 3
DJF	0.46 (0.41)	0.34 (0.29)	0.52 (0.43)	0.52 (0.51)
MAM	0.34 (0.29)	0.19 (-)	0.49 (0.48)	0.35 (0.32)
JJA	0.47 (0.43)	0.64 (0.61)	0.31 (0.23)	0.46 (0.45)
SON	0.31 (0.28)	0.33 (0.24)	0.16 (0.16)	0.45 (0.44)

<sup>a</sup>For the  $r$  values that are not in parentheses, the index is the difference of the area-averaged surface pressures between  $16^{\circ}\text{--}30^{\circ}\text{N} \times 147^{\circ}\text{--}160^{\circ}\text{E}$  and  $55^{\circ}\text{--}70^{\circ}\text{N} \times 147^{\circ}\text{--}160^{\circ}\text{E}$ . For the  $r$  values in parentheses, the index is the Honolulu–Anchorage pressure difference.



[52] Averages over seasonal ensembles at fixed transit time give the following seasonal-mean transport climate (Figures 2–5): During MAM, E-Asian air is particularly well exported from E-Asia and travels almost exclusively east toward N America. During JJA nearly half the E-Asian air moves westward aloft from Indochina to the Middle East. The climatology as well as event composites show that E-Asian air is lofted slantwise into the mid troposphere in DJF and MAM, consistent with warm-conveyor-belt transport and quasi-isentropic mixing. During JJA the upper atmosphere is directly accessed convectively, with SON being intermediate between JJA and DJF. During its transit across the Pacific, some of the lofted E-Asian air mass subsides over the Pacific High counteracting the dilution of E-Asian air propagating near the surface. E-Asian air older than  $\sim 2$  weeks likely reaches N America via a combination of downward transport from aloft and low-level horizontal transport, including advection from the Pacific surface pools that formed from earlier subsidence. Over western N America the E-Asian air arrives in the middle to upper troposphere first after 6–8 days for all seasons, although with pronounced seasonality in amplitude. The most probable transit time to the western N-American surface is  $\sim 2$  weeks for DJF, MAM, and SON, and  $\sim 3$  weeks for JJA. MAM produces the largest signal at the surface and throughout the troposphere over N America. During all seasons except MAM there is also rapid ( $\sim 2$ – $3$  days) transport to SE Asia (at lower levels in DJF, aloft in JJA, and both in SON).

[53] We have quantified transport variability in terms of the PW-averaged E-Asian air column. The E-Asian air-mass fraction displays weather-driven variability which depends strongly on the transit time since last  $\Omega$  contact. The structure of the variability of the PW E-Asian air burden is similar for all seasons, with the standard deviation having a nearly universal dependence on the mean when both are scaled by the seasonal-mean peak burden. Maximum variance occurs for a transit time of  $\sim 7$  days, several days before the mean itself reaches its maximum value. The variance then falls off in the tail of the pdf, roughly as a third of the mean. The fraction of days for which the PW burden of E-Asian air of age  $\tau$  or less exceeds a multiple of its seasonal mean is also only weakly dependent on season, although the seasonal means themselves differ strongly. The column burden aged 7 days or less approximately exceeds 1.5 times its seasonal mean 21% of the time. We plan to uncover the physical basis of the near-universal behavior of the variance with suitable idealized models in a separate study.

[54] We have defined weighted event and nonevent composites conditioned on the PW burden of 7-day old E-Asian air lagged by  $\tau$  days. When expressed as a perturbation from the seasonal mean state, the event composites reveal the average conditions that lead to large E-Asian air burdens over western N America. The weather systems associated with enhanced export from Asia are phased so that the exported air feeds into a second wind enhancement with a dipolar structure over the eastern Pacific. The strain-rate field of the dipole focuses the E-Asian air into a coherent air mass that is delivered to N America. This chain of events was already hinted at in a related analysis for spring by Holzer *et al.* [2003], but has been born out for all seasons in the present study. Our analysis suggests that

the merging of air streams of two baroclinic systems observed for a particular transport event by Cooper *et al.* [2004] is also a climatologically important process for transpacific transport. Nonevent composites show retention of the E-Asian air in the western Pacific with weakened mid-latitude westerlies and enhanced transport to Siberia during MAM. From an air-quality perspective it will be interesting to investigate in detail the conditions leading to large anomalies in the near-surface mixing ratio of transit-time segregated E-Asian air. We plan to focus on this in a future study that will further partition E-Asian air according to whether it was transported aloft or near the surface.

[55] The dipolar flow perturbations have a signature in the surface pressure. The PW burden of E-Asian air aged 14 days or less correlates with the local surface pressure lagged by two days with a pattern corresponding to an enhanced Aleutian Low and Pacific High. However, a daily Honolulu–Anchorage pressure index has only modest correlation with the daily PW burden two days later.

[56] While the focus of this paper has been transport from E Asia, it is useful to keep in mind that transpacific transport of Asian pollutants is but one facet of a global-scale phenomenon. There are well-documented episodes of long-range transport from all major pollution regions to “downwind” receptors across the northern hemisphere [e.g., Newell and Evans, 2000; Huntrieser *et al.*, 2005]. The Southern Hemisphere is comparatively clean, but pollutant transport from South Africa to Australia and New Zealand have also been documented [e.g., Piketh *et al.*, 2000; Wenig *et al.*, 2002]. In a future study we plan to decompose local air parcels not only according to their transit times from a fixed source region but also according to the parcel’s spatial surface footprint as a function of transit time so that transport becomes characterized by the joint probability of times and places since last surface contact.

[57] **Acknowledgments.** This work was supported by NSF grant ATM-04-32514. We thank Adam Sobel for discussions and the anonymous reviewers for their comments.

## References

- Berntsen, T. K., S. Karlsdottir, and D. A. Jaffe (1999), Influence of Asian emissions on the composition of air reaching the Northwestern United States, *Geophys. Res. Lett.*, **26**, 2171–2174.
- Bey, I. D., J. Jacob, M. Yantosca, J. A. Logan, B. D. Field, A. M. Fiore, Q. Li, H. Y. Liu, L. J. Mickley, and M. G. Schultz (2001), Global modeling of tropospheric chemistry with assimilated meteorology: Model description and evaluation, *Geophys. Res. Lett.*, **106**, 23,073–23,096.
- Cooper, O. R., *et al.* (2004), A case study of transpacific warm conveyor belt transport: Influence on merging airstreams on trace gas import to North America, *J. Geophys. Res.*, **109**, D23S08, doi:10.1029/2003JD003624.
- Hall, T. M., and R. A. Plumb (1994), Age as a diagnostic of stratospheric transport, *J. Geophys. Res.*, **99**, 1059–1070.
- Heald, C. L., *et al.* (2003), Asian outflow and trans-Pacific transport of carbon monoxide and ozone pollution: An integrated satellite, aircraft, and model perspective, *J. Geophys. Res.*, **108**(D24), 4804, doi:10.1029/2003JD003507.
- Holzer, M., and T. M. Hall (2000), Transit-time and tracer-age distributions in geophysical flows, *J. Atmos. Sci.*, **57**, 3539–3558.
- Holzer, M., I. G. McKendry, and D. A. Jaffe (2003), Springtime trans-Pacific atmospheric transport from east Asia: A transit-time-pdf approach, *J. Geophys. Res.*, **108**(D22), 4708, doi:10.1029/2003JD003558.
- Hudman, R. C., *et al.* (2004), Ozone production in transpacific Asian pollution plumes and implications for ozone air quality in California, *J. Geophys. Res.*, **109**, D23S10, doi:10.1029/2004JD004974.

- Huntrieser, H., et al. (2005), Intercontinental air pollution transport from North America to Europe: Experimental evidence from airborne measurements and surface observations, *J. Geophys. Res.*, **110**, D01305, doi:10.1029/2004JD005045.
- Husar, R. B., et al. (2001), Asian dust events of April 1998, *J. Geophys. Res.*, **106**, 18,317–18,330.
- Jacob, D. J., J. A. Logan, and P. P. Murti (1999), Effect of rising Asian emissions on surface ozone in the United States, *Geophys. Res. Lett.*, **26**, 2175–2178.
- Jacob, D. J., J. H. Crawford, M. M. Kleb, V. S. Connors, R. J. Bendura, J. L. Raper, G. W. Sachse, J. C. Gille, L. Emmons, and C. L. Heald (2003), The transport and chemical evolution over the Pacific (TRACE-P) aircraft mission: Design, execution, and first results, *J. Geophys. Res.*, **108**(D20), 9000, doi:10.1029/2002JD003276.
- Jaeglé, L., D. A. Jaffe, H. U. Price, P. Weiss-Penzias, P. I. Palmer, M. J. Evans, D. J. Jacob, and I. Bey (2003), Sources and budgets for CO and O<sub>3</sub> in the northeastern Pacific during the spring of 2001: Results from the PHOBEA-II experiment, *J. Geophys. Res.*, **108**(D20), 8802, doi:10.1029/2002JD003121.
- Jaffe, D., et al. (1999), Transport of Asian air pollution to North America, *Geophys. Res. Lett.*, **26**, 711–714.
- Jaffe, D., T. Anderson, D. Covert, B. Trost, J. Danielson, W. Simpson, D. Blake, J. Harris, and D. Streets (2001), Observations of ozone and related species in the northeast Pacific during the PHOBEA campaigns: 1. Ground based observations at Cheeka Peak, *J. Geophys. Res.*, **106**, 7449–7461.
- Jaffe, D., I. G. McKendry, T. Anderson, and H. Price (2003), Six ‘new’ episodes of trans-Pacific transport of air pollutants, *Atmos. Environ.*, **37**, 391–404.
- Kalnay, E., et al. (1996), The NMC/NCAR 40-year reanalysis project, *Bull. Am. Meteorol. Soc.*, **77**, 437–471.
- Kistler, R., et al. (2001), The NCEP/NCAR 50-year reanalysis, *Bull. Am. Meteorol. Soc.*, **82**, 247–267.
- Kotchenruther, R. A., D. A. Jaffe, H. J. Beine, T. L. Anderson, J. W. Bottenheim, J. M. Harris, D. R. Blake, and R. Schmitt (2001), Observations of ozone and related species in the northeast Pacific during the PHOBEA campaigns: 2. Airborne observations, *J. Geophys. Res.*, **106**, 7463–7483.
- Li, Q., D. J. Jacob, J. A. Logan, I. Bey, R. M. Yantosca, H. Liu, R. V. Martin, A. M. Fiore, B. D. Field, and B. N. Duncan (2001), A tropospheric ozone maximum over the Middle East, *Geophys. Res. Lett.*, **28**, 3235–3238.
- Liang, Q., L. Jaeglé, D. A. Jaffe, P. Weiss-Penzias, A. Heckman, and J. A. Snow (2004), Long-range transport of Asian pollution to the northwest Pacific: Seasonal variations and transport pathways of carbon monoxide, *J. Geophys. Res.*, **109**, D23S07, doi:10.1029/2003JD004402.
- Liang, Q., L. Jaeglé, and J. M. Wallace (2005), Meteorological indices for Asian outflow and transpacific transport on daily to interannual time-scales, *J. Geophys. Res.*, **110**, D18308, doi:10.1029/2005JD005788.
- Liu, H., D. J. Jacob, I. Bey, R. M. Yantosca, B. N. Duncan, and G. W. Sachse (2003), Transport pathways for Asian pollution outflow over the Pacific: Interannual and seasonal variations, *J. Geophys. Res.*, **108**(D20), 8786, doi:10.1029/2002JD003102.
- Liu, J., D. L. Mauzerall, and L. W. Horowitz (2005), Analysis of seasonal and interannual variability in transpacific transport, *J. Geophys. Res.*, **110**, D04302, doi:10.1029/2004JD005207.
- McKendry, I. G., J. P. Hacker, R. Stull, S. Sakiyama, D. Mignacca, and K. Reid (2001), Long-range transport of Asian dust to the Lower Fraser Valley, British Columbia, Canada, *J. Geophys. Res.*, **106**, 18,361–18,370.
- Merrill, J. T., M. Uematsu, and R. Bleck (1989), Meteorological analysis of long-range transport of mineral aerosols over the North Pacific, *J. Geophys. Res.*, **94**, 8584–8598.
- Newell, R. E., and M. J. Evans (2000), Seasonal changes in pollutant transport to the North Pacific: The relative importance of Asian and European sources, *Geophys. Res. Lett.*, **27**, 2509–2512.
- Parrish, D. D., Y. Kondo, O. R. Cooper, C. A. Brock, D. A. Jaffe, M. Trainer, T. Ogawa, G. Hübner, and F. C. Fehsenfeld (2004), Intercontinental Transport and Chemical Transformation 2002 (ITCT 2K2) and Pacific Exploration of Asian Continental Emission (PEACE) experiments: An overview of the 2002 winter and spring intensives, *J. Geophys. Res.*, **109**, D23S01, doi:10.1029/2004JD004980.
- Piketh, S., P. Tyson, and W. Steffen (2000), Aeolian transport from southern Africa and iron fertilization of marine biota in the South Indian Ocean, *S. Afr. J. Sci.*, **96**, 244–246.
- Price, H. U., D. A. Jaffe, P. Doskey, I. G. McKendry, and T. Anderson (2003), Vertical profiles of O<sub>3</sub>, aerosols, CO, and NMHCs in the northeast Pacific during the ACE-ASIA and TRACE-P experiments, *J. Geophys. Res.*, **108**(D20), 8799, doi:10.1029/2002JD002930.
- Rasch, P. J., and M. Lawrence (1998), Recent developments in transport methods at NCAR, in *MPI Workshop on Conservative Transport Schemes*, 265, pp. 65–75, Max-Planck-Inst. for Meteorol., Hamburg, Germany.
- Rasch, P. J., N. M. Mahowald, and B. E. Eaton (1997), Representations of transport, convection and the hydrologic cycle in chemical transport models: Implications for the modeling of short lived and soluble species, *J. Geophys. Res.*, **102**, 28,127–28,138.
- Stohl, A. (2001), A one-year Lagrangian “climatology” of airstreams in the northern hemisphere troposphere and lowermost stratosphere, *J. Geophys. Res.*, **106**, 7263–7279.
- Stohl, A., S. Eckhardt, C. Forster, P. James, and N. Spichtinger (2002), On the pathways and timescales of intercontinental air pollution transport, *J. Geophys. Res.*, **107**(D23), 4684, doi:10.1029/2001JD001396.
- Tratt, D. M., R. J. Frouin, and D. L. Westphal (2001), April 1998 Asian dust event: A southern California perspective, *J. Geophys. Res.*, **106**, 18,371–18,379.
- Uno, I., H. Amano, S. Emori, K. Kinoshita, I. Matsui, and N. Sugimoto (2001), Transpacific yellow sand transport observed in April 1998: A numerical simulation, *J. Geophys. Res.*, **106**, 18,331–18,344.
- Vaughan, J. K., C. Claiborn, and D. Finn (2001), April 1998 Asian dust event over the Columbia Plateau, *J. Geophys. Res.*, **106**, 18,381–18,402.
- Wenig, M., N. Spichtinger, A. Stohl, G. Held, S. Beirle, T. Wagner, B. Jähne, and U. Platt (2002), Intercontinental transport of nitrogen oxide pollution plumes, *Atmos. Chem. Phys.*, **3**, 387–393.
- Yienger, J. J., M. Galanter, T. A. Holloway, M. J. Phadnis, S. K. Guttikunda, G. R. Carmichael, W. J. Moxim, and H. Levy II (2000), Episodic nature of air pollution transport from Asia to North America, *J. Geophys. Res.*, **105**, 26,931–26,945.

T. M. Hall and M. Holzer, NASA Goddard Institute for Space Studies, 2880 Broadway, New York, NY 10025, USA. (thall@giss.nasa.gov; mholzer@eos.ubc.ca)

R. B. Stull, Department of Earth and Ocean Sciences, University of British Columbia, 6339 Stores Road, Vancouver, BC, Canada V6T 1Z4. (rstull@eos.ubc.ca)